catalysts

MDPI

Article

Kinetics of Fischer–Tropsch Synthesis in a 3-D Printed Stainless Steel Microreactor Using Different Mesoporous Silica Supported Co-Ru Catalysts

Nafeezuddin Mohammad [1], Sujoy Bepari [2], Shyam Aravamudhan [1] and Debasish Kuila [1,2,*]

[1] Department of Nanoengineering, Joint School of Nanoscience and Nanoengineering, North Carolina A&T State University, Greensboro, NC 27411, USA; nmohammad@aggies.ncat.edu (N.M.); saravamu@ncat.edu (S.A.)

[2] Department of Chemistry, North Carolina A&T State University, Greensboro, NC 27411, USA; sbepari@ncat.edu

* Correspondence: dkuila@ncat.edu; Tel.: +1-336-285-2243

Received: 14 September 2019; Accepted: 15 October 2019; Published: 21 October 2019

Abstract: Fischer–Tropsch (FT) synthesis was carried out in a 3D printed stainless steel (SS) microchannel microreactor using bimetallic Co-Ru catalysts on three different mesoporous silica supports. CoRu-MCM-41, CoRu-SBA-15, and CoRu-KIT-6 were synthesized using a one-pot hydrothermal method and characterized by Brunner–Emmett–Teller (BET), temperature programmed reduction (TPR), SEM-EDX, TEM, and X-ray photoelectron spectroscopy (XPS) techniques. The mesoporous catalysts show the long-range ordered structure as supported by BET and low-angle XRD studies. The TPR profiles of metal oxides with H_2 varied significantly depending on the support. These catalysts were coated inside the microchannels using polyvinyl alcohol and kinetic performance was evaluated at three different temperatures, in the low-temperature FT regime (210–270 °C), at different Weight Hourly Space Velocity (WHSV) in the range of 3.15–25.2 kgcat.h/kmol using a syngas ratio of $H_2/CO = 2$. The mesoporous supports have a significant effect on the FT kinetics and stability of the catalyst. The kinetic models (FT-3, FT-6), based on the Langmuir–Hinshelwood mechanism, were found to be statistically and physically relevant for FT synthesis using CoRu-MCM-41 and CoRu-KIT-6. The kinetic model equation (FT-2), derived using Eley–Rideal mechanism, is found to be relevant for CoRu-SBA-15 in the SS microchannel microreactor. CoRu-KIT-6 was found to be 2.5 times more active than Co-Ru-MCM-41 and slightly more active than CoRu-SBA-15, based on activation energy calculations. CoRu-KIT-6 was ~3 and ~1.5 times more stable than CoRu-SBA-15 and CoRu-MCM-41, respectively, based on CO conversion in the deactivation studies.

Keywords: Fischer-Tropsch synthesis; mesoporous silica based catalysts; kinetic studies; 3-D printed microchannel microreactor

1. Introduction

Although Fischer–Tropsch (FT) synthesis was discovered by Franz Fischer and Hans Tropsch in the 1920s in Germany [1], it has gained immense attention in last few years due to depletion of non-renewable energy sources. FT synthesis is an environmental friendly route for alternative fuels and can produce liquid fuels from carbon sources by coal-to-liquid (CTL), natural gas-to-liquid (GTL) and biomass-to-liquid (BTL) [2] processes. Three types of reactors have been utilized commercially for FT synthesis: Fixed bed, fluidized bed, and slurry bubble column bed by leading GTL companies like Shell, Sasol, Exxon Mobil, and Energy Int. [3]. There is a minimum scale limit of this FT process to be economical; for example, the Pearl GTL, a collaboration between Shell and Qatar petroleum, producing 140,000 bpd (barrels per day) is considered as a profitable economic scale for the FT GTL

process [4]. The limitation of the scale-up considerations to commercialize small scale plants to be more profitable has driven industries and researchers to pursue an interest in alternative technologies. Since FT synthesis is highly exothermic in nature, there is a need for much process intensification technologies. The microreactor platform, which contains microstructured units called microreactors, uses a large number of small, parallel channels with different channel designs. This technology provides an alternative platform for controlling highly exothermic reactions like FT synthesis with enhanced mass and heat transfer. It has gained much attention in process intensification of FT synthesis [5,6] as isothermal operating conditions are well maintained in a microreactor with good control over process parameters which favors quick screening of catalyst for different chemical reactions. The reaction zone for these microreactors are several parallel microchannels with small geometry. The specific surface area of the reaction zone is greatly enhanced by the design of microchannels resulting in an efficient FT synthesis. In addition to efficient heat and mass transfer with good heat dissipation, microreactors also have advantages such as high reaction throughput, easy scale-up, good portability, and lower cost over conventional reactors [6–10]. This has been demonstrated commercially and in R&D by Velocys and Micrometrics Corporations [11–14].

Iron, cobalt, and ruthenium catalysts have been extensively used for FT synthesis [15]. To increase the performance of catalysts, different supports have been used; some of the previous studies examined the role of Al_2O_3 [16–20], TiO_2 [21–28], SiO_2 [29–33], and CNTs [34–36] as supporting materials for the formation of higher alkanes. These supports tend to enhance the FT process by increasing the active number of catalytic sites and good metal dispersion with the high surface area. Therefore, the selection of support and study of its interaction with the incorporated metal ion plays an important role in catalysis. In our previous studies, sol-gel encapsulated catalysts were used in silicon microreactors for FT synthesis [37–39]. While Al_2O_3 and SiO_2 sol-gel supports show similar behavior in formation of higher alkanes such as ethane, propane, and butane for the reactions at 1 atm, TiO_2 has a profound effect on FT synthesis [40] and the stability of the catalysts are observed in reverse order from that observed with SiO_2 and Al_2O_3. However, in all these studies, sol-gel coated catalysts in silicon microreactors tend to have challenges such as low surface area, clogging of microchannels and difficulty in reducing the metal oxides to expose active sites. In addition, the Si-microreactors are fragile and they break easily and require a large infrastructure for fabrication. Further, it's more difficult to increase pressure for FT studies using Si-microreactors. Thus, we have turned our attention to 3D printed stainless steel (SS) microreactors which are easy to fabricate by direct metal laser sintering *layer-by-layer* additive manufacturing technique. Recently, 3D printed microreactors have been used as flow devices in many chemical reactions such as fast difluoromethylation [41], a customizable Lab-On-Chip device for optimization of carvone semicarbazon [42], a micro fuel cell [43,44], and wide range of organic and inorganic reactions [45–47]. Further, these metal printed microreactors have been used for high pressure and temperature chemical reactions providing a new fast developing reactor technology in process development to industrial scale [47], which makes them suitable for reactions like FT synthesis due to its good mechanical and thermal properties. Although the specific surface area of stainless steel microreactor is less when compared to silicon microreactors used in our previous studies [40], the use of stainless steel material increases heat transfer, its chemical and mechanical resistances play a major role in process intensification of chemical processes. In order to increase specific surface area of the reaction zone in microreactors, we synthesized catalysts with surface area greater than 1000 m^2/g using mesoporous MCM-41 support. The use of high surface area MCM-41 for FT catalysis stems from our previous studies, which can be prepared easily by one-pot hydrothermal procedure and are extremely stable, for steam reforming of methanol to produce hydrogen [48–51]. Bimetallic catalysts containing Co and one other metal—Fe, Ru, or Ni—were prepared to investigate the synergistic effect of bi-metallic species on the FT performance (manuscript submitted), The results show that CoRu-MCM-41 is more active than other bimetallic catalysts in producing longer-chain hydrocarbons at one atmosphere.

In this manuscript, we have focused on the kinetics of FT synthesis in a 3-D printed Stainless Steel(SS) microreactor using CoRu bimetallic catalysts supported by MCM-41, and two other mesoporous silica supports: SBA-15 and KIT-6. In order to translate new advancements in the laboratory as well as industry on both catalysis and microreactors for FT synthesis, chemical kinetics is a key issue in developing mathematical models for the reactors. However, to our knowledge, the kinetics of FT synthesis using mesoporous materials in a microreactor is relatively unknown in the literature. So, in order to understand more about the interaction between silica mesoporous materials and the metal, and especially kinetics, three different types of silica mesoporous materials (MCM-41, SBA-15, and KIT-6) containing cobalt and ruthenium metals were synthesized by one-pot hydrothermal method. To address the thermodynamic stability of the catalysts, CO-conversion using these three catalysts in the 3-D printed SS microchannel microreactor was also investigated.

2. Results and Discussion

2.1. Catalyst Characterization

2.1.1. Textural Evaluation of Catalysts

The textural properties of the catalysts were evaluated using nitrogen Brunner–Emmett–Teller (BET) physisorption analysis. Table 1 shows the BET surface area, pore volume and the average pore diameter of all three catalysts. The surface areas of the catalysts are different depending upon the type of silica support. While the surface area of CoRu-MCM-41 was 1025 m^2/g, that of CoRu-SBA-15 and CoRu-KIT-6 was around 691 m^2/g and 690 m^2/g, respectively. The general trend is consistent with that reported in the literature [48,52,53]. The pore diameter in the range of 3.2–5.3 nm was obtained from BJH desorption plot. The pore volume was in the range of 0.77–0.92 cm^3/g. Figure 1a shows nitrogen adsorption–desorption isotherms for all the catalysts with pore size distribution of mesoporous materials. These isotherms represent the category of Type IV isotherms which is typical for mesoporous materials as mentioned in IUPAC classification [54]. These isotherms are classified into three different types of regions. The initial part of isotherm is a linear increment of nitrogen uptake at lower relative pressures (P/P_0 = 0–0.2) called Type II isotherm. This is due to the adsorption of N_2 on monolayer and multilayer within the pore walls of the catalyst. For relative pressure in the range of P/P_0 = 0.2–0.4, there is an exponential increment in the isotherms which indicates the ordered mesoporous structure of the catalysts. Especially, the steepness of CoRu-MCM-41 is sharp when compared to the other two samples which indicate that MCM-41 support is more ordered in the nature of all the catalysts. Finally, the third region, in the relative pressure range of P/P_0 = 0.4–0.95, has a long plateau for all the catalysts and it corresponds to the multilayer adsorption on the outer surface of the catalyst. The hysteresis loop for the samples is associated with condensation of N_2 uptake in the interstitial voids of mesopores of the support [55]. Figure 1b shows pore size distribution obtained from BJH desorption plots. A sharp single peak for pore size with narrow distribution is observed for all the catalysts covering uniformly the pores with sizes in the range of 3.2 to 5.3 nm as shown in Table 1. The pore sizes of KIT-6 support appear to be larger and wider when compared to that of MCM-41 and SBA-15 supports. Furthermore, the pore distribution of MCM-41 is bi-modal, having major pores distributed in the range of 2 to 3 nm and minimal pore distribution between 3–4 nm.

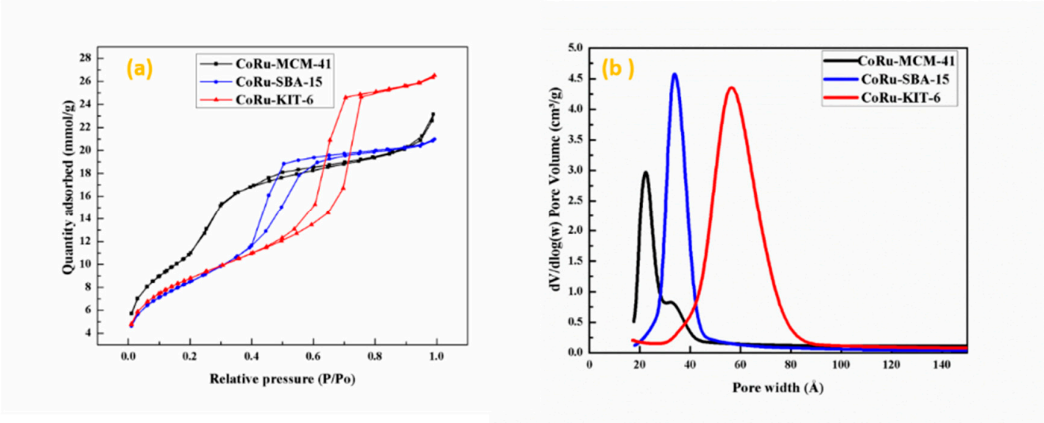

Figure 1. (**a**) N_2 adsorption–desorption isotherms of CoRu-S (S = MCM-41, SBA-15, KIT-6) and (**b**) pore size distribution of the catalyst.

Table 1. Brunner–Emmett–Teller (BET) surface area, pore size, pore volume and EDX metal loadings of synthesized catalysts.

Mesoporous Silica Supported Catalyst with Intended Metal Loadings	Surface Area [a] (m^2/g)	Pore Volume [b] (cm^3/g)	Pore Size [c] (nm)	Metal Loadings Obtained from SEM-EDX (wt %)
10% Co5%Ru-MCM-41	1025	0.77	3.2	9%Co3.9%Ru-MCM-41
10% Co5%Ru-SBA-15	691	0.73	4.2	8.4%Co4.5%Ru-KIT-6
10%Co5%Ru-KIT-6	690	0.92	5.3	11.1%Co5.6%Ru-SBA-15

[a] = Variation range ±2%, [b] = Variation range ±3%, [c] = Variation range ±5%.

2.1.2. SEM-EDX Analysis

The metal loadings in the catalysts (wt%) and the surface morphology were obtained by SEM-EDX analysis. Figure S1 shows the SEM-EDX images of a typical MCM-41 catalyst showing uniform metal distribution with porous morphology. The actual and intended metal loadings are quite similar (Table 1) and suggest that the one-pot hydrothermal synthesis is one of the best routes to prepare mesoporous materials with uniform metal distribution. This uniformity plays a key role in the activity of FT catalysts; it not only decreases sintering but also increases the thermal stability of the catalysts for long-term studies.

2.1.3. Transmission Electron Microscopic (TEM) Imaging

The size of the metal particles and the structure of the mesoporous support in all catalysts were obtained from TEM studies. The high magnification images in Figure 2 show the uniform ordered hexagonal pores present in the support. It is also worth noting that MCM-41 support has well defined hexagonal pores when compared to KIT-6 and SBA-15 and this is consistent with the BET surface area and the low angle XRD studies (discussed below). A uniform metal distribution with black dots, as shown in Figure S2, having almost circular in shape is clearly evident in the mesoporous silica matrix.

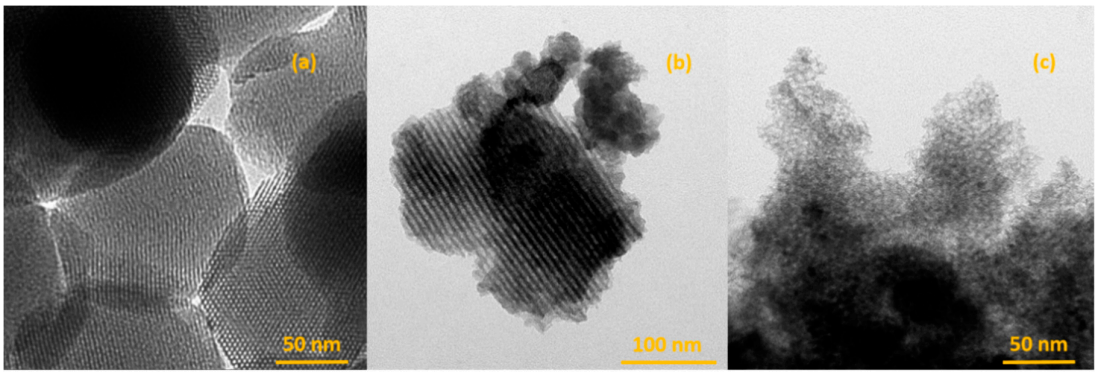

Figure 2. High magnification TEM images of CoRu-S Catalysts (S = (**a**) MCM-41, (**b**) SBA-15, (**c**) KIT-6.

2.1.4. Powder X-Ray Diffraction (XRD) Studies of Calcined Catalysts

In order to obtain information about the structural phases of the catalysts, XRD studies were carried out. Figure 3 shows the small angle XRD diffraction patterns for different mesoporous silica supported catalysts. The variations of peaks are probably due to the presence of metal nanoparticles present in the catalyst. For CoRu-MCM-41 catalyst, a sharp intense peak between 2-theta values 2–3° and two broad peaks between 2-theta values 4–5.5° corresponds to (100), (110), and (200) reflections of hexagonal mesoporous structure. This confirms that these catalysts are highly ordered mesoporous in nature with no deformation of hexagonal framework even after the addition of metals and this is consistent with the observed TEM images. For CoRu-SBA-15 catalyst, the peak between 2-theta value 1–2° indicates the mesoporous structure with 2D hexagonal symmetry with p6mm space group and long range ordered mesoporous structure [56]. For CoRu-KIT-6 catalyst, the peak at 2-theta value 0.94° corresponds to (211) plane and two low intensity peaks between 1.5–2° ascribes to (420) and (332) diffraction planes. These planes confirmed the characteristic three-dimensional nature of mesoporous KIT-6 reported in the literature [57].

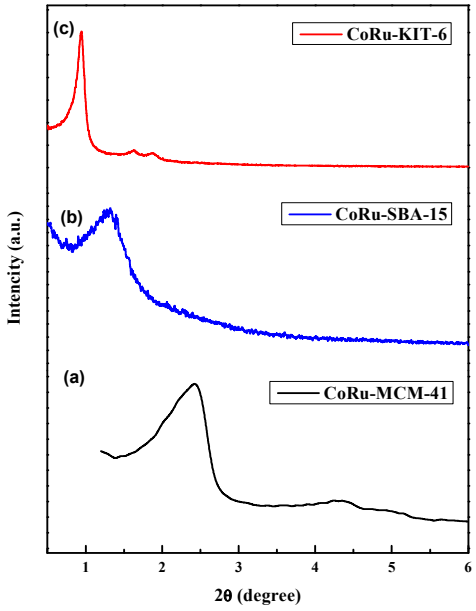

Figure 3. Low angle XRD of three bimetallic mesoporous catalysts: (**a**) CoRu-MCM41; (**b**) CoRu-SBA15; (**c**) CoRu-KIT6.

The wide-angle XRD (WAXRD) analysis was carried out to determine the crystallinity of metal oxides in different mesoporous supports. Figure 4 shows the WAXRD patterns of these samples. The observed 2θ angles are compared with the JCPDS (Joint Committee on Powder Diffraction Standards) database. For all catalysts, the peaks at 18.90° (111), 31.09° (220), 36.74° (311), 38.36° (222), 44.72° (400), 59.25° (511), and 65.26° (440) correspond to the cubic structure of Co_3O_4 (JCPDS-42-1467) [58, 59]. The orthorhombic structure of RuO_2 (JCPDS-88-0323) is consistent with the observed peaks at 28.18° (110), 35.27° (101), and 54.56° (211) in all the catalysts.

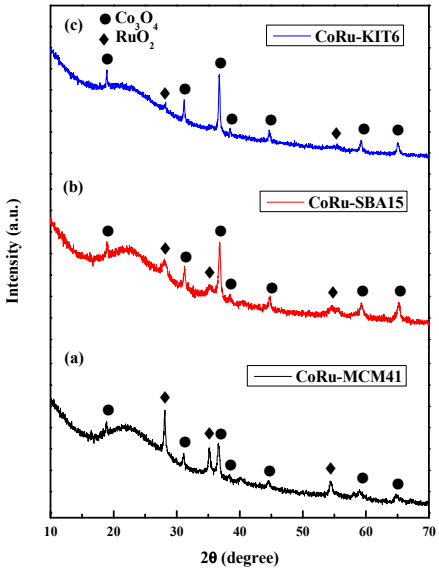

Figure 4. Wide angle XRD patterns of three bimetallic catalysts: (**a**) CoRu-MCM41; (**b**) CoRu-SBA15; (**c**) CoRu-KIT6.

2.1.5. X-Ray Photoelectron Spectroscopy (XPS)

To determine the oxidation states of Co and Ru in MCM-41, KIT-6, and SBA-15, XPS studies were performed. Figure S3 shows the XPS spectra of Si 2p and O 1s containing a single spectrum which is centered at 104 eV and 532 eV, respectively, and confirms the presence of silicates in the sample. Figure 5a shows the Co 2p spectra for all the samples; the Co $2p_{3/2,}$ and Co $2p_{1/2}$ peaks are clearly observed to indicate the presence of cobalt in two oxidation states in the silica matrix [60-62]. The peaks centered at 780.5 eV and 796.2 eV are associated with Co $2p_{3/2}$ and Co $2p_{1/2}$, respectively in the MCM-41 matrix. Whereas, in the case of KIT-6, the peaks for Co $2p_{3/2}$ and Co $2p_{1/2}$ are observed at 779.6 eV and 795.8 eV, respectively. For SBA-15, the similar peaks are noticed at 779.7 eV and 794.8 eV, respectively. It is clear from these data that the binding energy for cobalt in the MCM-41 matrix is distinctly higher when compared to that of cobalt in KIT-6 and SBA-15. This suggests that cobalt in two oxidation states in MCM-41 is in a different environment from that of SBA-15 and KIT-6. This is also consistent with temperature programmed reduction (TPR) profile showing much higher reduction temperatures for CoRu-MCM-41 catalyst as discussed below. Similar XPS spectra for Co 2p were observed and analyzed by Bhoware et al., [63]. Figure 5b shows the XPS spectra for the ruthenium metal in the catalyst. The presence of Ru in the sample is confirmed by the Ru 3d spectra which is centered almost at 284.8 eV and it is associated with the Ru $3d_{3/2}$ oxidation state [64]. However, in contrast to cobalt, there is no significant difference in the binding energy of the Ru metal ions in different mesoporous silica supports.

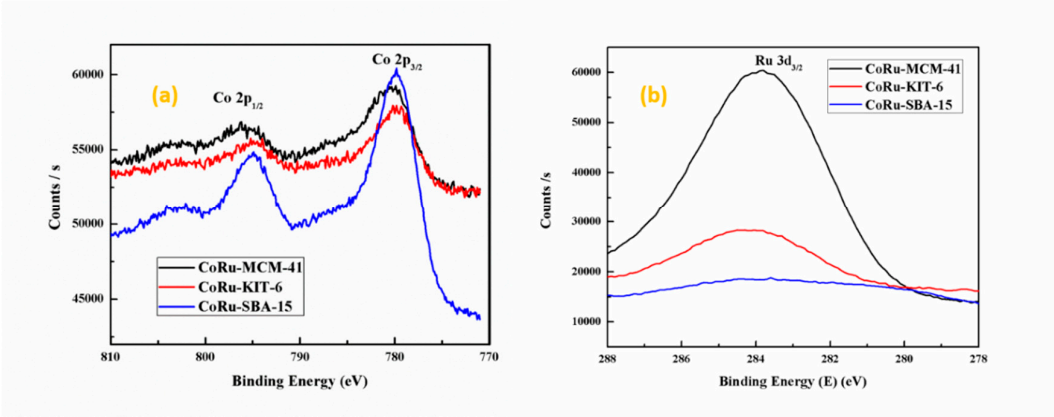

Figure 5. XPS spectra of metals incorporated MCM-41, KIT-6, and SBA-15: (**a**) Co 2p spectra and (**b**) Ru 3d spectra.

2.1.6. H_2 Temperature Programmed Reduction (H_2 TPR)

Temperature programmed reduction (TPR) is an ideal technique to analyze the reduction behavior of metal oxides in mesoporous silica. It helps to investigate the interaction between metal and the support by providing information on physiochemical properties of the material. All the calcined catalysts are treated with 10%H_2 to record TPR profiles for Co and Ru metal oxides shown in Figure 6. All the samples contain well defined peaks for ruthenium at low reduction temperatures and cobalt at much higher reduction temperatures. The TPR profiles of all the catalysts show that the ruthenium oxide is reduced with H_2 at a relatively lower temperature between 100 °C and 250 °C with main hydrogen consumption peaks for Ru^{3+} to Ru^0 which is also reported by Panpranot et al. [65]. However, the reduction behavior of Co_3O_4 ($Co_3O_4 \rightarrow CoO \rightarrow Co^0$) [66] in three samples to Co^0 is remarkably different depending on the type of support. For MCM-41, as reported by Lim et al., the small peak centered around 310 °C ascribes the reduction of cobalt to CoO, while the second main peak corresponds to the reduction of CoO to metal ions Co^{2+} into the silica network [67]. The last hydrogen uptake has a peak centered almost 780 °C which suggests that the cobalt and the MCM-41 support have strong interaction which is also confirmed by the binding energy obtained from XPS in Figure 5a [48,68]. This could be due to the formation of a spinel structure as cobalt silicates [69] and consistent with the XPS and XRD data. Unlike MCM-41, the reduction temperatures of Co inSBA-15 and KIT-6 were quite low around 365 °C and 375 °C, respectively, confirming weaker metal interactions with SBA-15 and KIT-6 supports [53]. However, no separate three peaks were observed for the reduction of cobalt, this may be due to the absence of silicates in SBA-15 and KIT-6 samples. The shift in the reduction peaks to the lower temperatures can also be due to the incorporation of Ru metal in the support [70]. Although the 5% weight of Ru is maintained in the catalyst sample, there might be a slight difference in the actual loadings of the Ru metal as shown in EDX Table 2. Qin et al., have studied the effect of the Ru metal on Co-SBA-15 catalyst at different loading and found a remarkable effect on the activity of catalyst during the FT synthesis [70]. Thus, the overall interactions of metal–metal and metal–support have a strong influence on the reducibility and reactivity of the catalysts for FT synthesis. Since the operating temperature zone of the FT synthesis is less than 350 °C, the activity of the catalyst is more dependent on the ease of reducibility of the metal oxides to pure metals (active sites) in the support.

The amount of hydrogen consumed by CoRu-MCM-41, CoRu-SBA-15, and CoRu-KIT-6 catalysts was calculated and quantified to be 0.108, 0.05, and 0.032 mmol H_2/gm, respectively in the temperature range of 25 to 1000 °C. The amount of hydrogen consumed by CoRu-MCM-41 was found almost two times more than that of CoRu-SBA-15 and 3 times more than by CoRu-KIT-6. Higher hydrogen uptake by CoRu-MCM-41 is most likely due to the reduction of Co-silicates ~750 °C.

Although MCM-41 exhibits higher hydrogen consumption than other catalysts, the amount of hydrogen adsorbed by CoRu-KIT-6 in the temperature range of 25–311 °C is higher when compared to that by CoRu-MCM-41 and CoRu-SBA-15 in the same range of temperature.

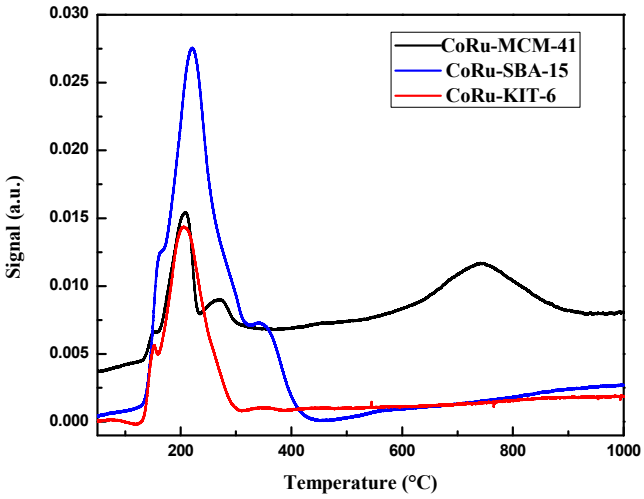

Figure 6. H_2-TPR(temperature programmed reduction) profiles of CoRu-S (S = MCM-41, KIT-6 and SBA-15) Catalysts

2.2. FT Reaction Mechanism

In order to have a better understanding of the effect of metal and support interaction on catalysts, kinetic studies were carried out in the SS microchannel microreactors. The main difficulty to describe the FT kinetics is the complexity of its mechanism and a larger number of possible chemical species involved. Kinetic models of FT synthesis using Co based catalysts are less abundant than Fe based catalysts in literature [71]. Most of the existing models are mainly based on power-law models where Langmuir–Hinselwood (LH) type equations have been used by different researchers [72–76]. Although the simple power-law expression is widely recognized in the field of catalysis, it was recognized to have limited application in FT synthesis due to the narrow range of reaction conditions [77,78]. However, LH type equations are widely used for prediction of rates over a wide range of reaction conditions. As an example, Yates and Satterfield [72] worked on Co-catalyst and fitted the rate data obtained at 220–240 °C. They found that the rate data were best fitted with simple LH expression. Rautavuoma and van dar Baan [79] reported the rate of reaction at 1 atm pressure and 250 °C. They observed that reaction proceeds through CO dissociation and formation of -CH_2- surface intermediate.

2.2.1. Reaction Mechanism

In the microchannels of the microreactor, the flow of reactants is basically laminar. The complexity of the microchannel microreactor increases due to the parabolic type velocity profile; so, an average velocity profile is approximated during the development of the model for the microreactor system [80]. The outlet concentrations of the limiting reactant (CO), which was related to the rate of reaction, were calculated by an in-line GCMS. The following differential equation was used for a reactor model defined as Equation (1):

$$\frac{W_{cat}}{F_{in,CO}} = \int_{X_{CO,in}}^{X_{CO,out}} \frac{dX_{CO}}{-r_{CO}} \quad (1)$$

W_{cat} = Wt. of the catalyst

$F_{in,CO}$ = Molar feed rate of CO

X_{CO} = Conversion of CO

$-r_{CO}$ = Disappearance rate of CO

Equation (2), below, is used to calculate the disappearance rate of CO

$$-r_{CO} = \frac{X_{CO} F_{in,CO}}{W_{cat}} \quad (1)$$

The following boundary conditions (BC) were used:

$W = 0$; $F_i = F_{i(inlet)}$

$W = W_{cat}$; $F_i = F_{i(exit)}$

The partial pressure of the compound was calculated using the following equations:

$$p_i = \frac{m_i}{\sum_{i=1}^{N_c} m_i} P_T \quad (2)$$

where p_i is the partial pressure of the component, P_T is the total pressure of the reactor at the inlet (1 atm) and N_c is the total number of components. m_i is the number of moles of component i.

2.2.2. Mechanism and Kinetics

In order to determine the most suitable kinetic model for a particular catalyst, all possible combinations of FT reactions were considered and rate equations were developed based on CO conversion. A number of Langmuir–Hinshelwood and Eley–Rideal models have been developed for kinetics of CO hydrogenation to hydrocarbons in different types of reactors over the past few years [80–82]. In this study, it was assumed that the FT reactions occur only at active sites and proposed six possible mechanisms for FT reactions to develop kinetic models in the microchannel microreactor as shown in Table 2. In order to derive an appropriate model that describes a suitable FT equation, we considered six cases with different elementary reaction steps for each case as shown in Table 2.

Table 2. Elementary reaction steps for Fischer–Tropsch synthesis.

Model	No	Elementary Reaction
FT-1	1	$CO + * \underset{k_{-1}}{\overset{k_1}{\rightleftharpoons}} CO* \quad K_1 = \frac{k_1}{k_{-1}}$
	2	$CO* + H_2 \xrightarrow{k} C + D + *$
FT-2	1	$H_2 + * \underset{k_{-1}}{\overset{k_1}{\rightleftharpoons}} H_2* \quad K_1 = \frac{k_1}{k_{-1}}$
	2	$H_2* + CO \xrightarrow{k} C + D + *$
FT-3	1	$CO + * \underset{k_{-1}}{\overset{k_1}{\rightleftharpoons}} CO* \quad K_1 = \frac{k_1}{k_{-1}}$
	2	$H_2 + * \underset{k_{-2}}{\overset{k_2}{\rightleftharpoons}} H_2* \quad K_2 = \frac{k_2}{k_{-2}}$

	3	$CO^* + H_2^* \xrightarrow{k} C + D + 2^*$
FT-4	1	$CO + * \rightleftharpoons CO^* \quad K_1 = \frac{k_1}{k_{-1}}$
	2	$CO^* + H_2 \rightleftharpoons COH_2^* \quad K_2 = \frac{k_2}{k_{-2}}$
	3	$COH_2^* \xrightarrow{k} C + D + *$
FT-5	1	$H_2 + * \rightleftharpoons H_2^* \quad K_1 = \frac{k_1}{k_{-1}}$
	2	$H_2^* + CO \rightleftharpoons COH_2^* \quad K_2 = \frac{k_2}{k_{-2}}$
	3	$COH_2^* \xrightarrow{k} C + D + *$
FT-6	1	$CO + * \rightleftharpoons CO^* \quad K_1 = \frac{k_1}{k_{-1}}$
	2	$H_2 + * \rightleftharpoons H_2^* \quad K_2 = \frac{k_2}{k_{-2}}$
	3	$CO^* + H_2^* \rightleftharpoons COH_2^* + * \quad K_3 = \frac{k_3}{k_{-3}}$
	4	$COH_2^* \xrightarrow{k} C + D + *$

In FT-1, CO is adsorbed on active site (*) of catalyst to form a CO* intermediate. Then, CO* reacts with H_2 to give the products C (hydrocarbons) and D (H_2O). Similarly, H_2 can be adsorbed on the catalyst site (*) to form H_2* intermediate and this intermediate subsequently reacted with CO to yield products in the FT-2 mechanism. There are two steps of adsorption in the FT-3 mechanism. In 1st and 2nd steps, CO and H_2 both are adsorbed on catalyst active site (*) to form two intermediates (CO* and H_2*). In the last step (surface reaction), these two intermediates react with each other to give products C and D. The FT-4 model consisted of three different steps. In the 1st step (adsorption), CO is adsorbed on catalyst site (*) to form CO*. In 2nd step (surface reaction), the intermediate (CO*) reacts with H_2 to form another intermediate (COH_2*). In the last step (desorption), the final intermediate gave products (C and D). Like FT-4, FT-5 also consists of three different steps—adsorption, surface reaction, and desorption. In the 1st step (adsorption), H_2 is adsorbed on catalyst site (*) to form the H_2* intermediate. This intermediate reacts with CO to form another intermediate (COH_2*) in the 2nd step (surface reaction). In 3rd step, the products (C and D) are formed from the intermediate (COH_2*). In contrast to other models, FT-6 consists of four different steps. The 1st and 2nd steps are like that of the FT-3 mechanism. The 3rd step is the surface reaction where two intermediates (CO* and H_2*) react with each other to give another intermediate COH_2* and released one active site (*). In last step (desorption), the intermediate (COH_2*) yields products (C and D).

Using the six models described above, six rate equations can be deduced for FT reactions by considering surface reaction and rate-limiting desorption as shown in Table 3. (See Appendix A for the rate equation derived using the FT-3 kinetic model).

Table 3. Proposed kinetic equations for Fischer–Tropsch synthesis.

Model	Rate Controlling Step (RCS)	Kinetic Equation

FT-1	(2)	$-r_{CO} = \frac{kK_1 p_{CO} p_{H_2}}{(1 + K_1 p_{CO})}$
FT-2	(2)	$-r_{CO} = \frac{kK_1 p_{CO} p_{H_2}}{(1 + K_1 p_{H_2})}$
FT-3	(3)	$-r_{CO} = \frac{kK_1 K_2 p_{CO} p_{H_2}}{(1 + K_1 p_{CO} + K_2 p_{H_2})^2}$
FT-4	(3)	$-r_{CO} = \frac{kK_1 K_2 p_{CO} p_{H_2}}{(1 + K_1 K_2 p_{CO} p_{H_2} + K_1 p_{CO})}$
FT-5	(3)	$-r_{CO} = \frac{kK_1 K_2 p_{CO} p_{H_2}}{(1 + K_1 K_2 p_{CO} p_{H_2} + K_1 p_{H_2})}$
FT-6	(4)	$-r_{CO} = \frac{kK_1 K_2 K_3 p_{CO} p_{H_2}}{(1 + K_1 K_2 K_3 p_{CO} p_{H_2} + K_1 p_{CO} + K_2 p_{H_2})}$

All the models presented in Table 3 were verified against experimental data to obtain the best suitable mechanism with the best fit. The models FT-1, FT-2, FT-4, and FT-5 are based on Eley–Rideal-type mechanism. In this case, one reactant gets adsorbed and another reactant reacts directly from the gas phase to form intermediates that yield products. Other models FT-3 and FT-6 are based on the Langmuir–Hinshelwood mechanism, which means all reactants are adsorbed on the catalyst surface before the products are formed. The kinetic parameter (k) and equilibrium constants (K_1, K_2, K_3) at each temperature were evaluated by non-linear regression analysis based on Levenberg–Marquart algorithm in POLYMATH software by minimizing the sum of squared residuals of reaction rates [83,84]. The objective function is defined as:

$$F = \sum_{i=1}^{N} \left(\mathrm{r}_{cal_i} - \mathrm{r}_{\exp_i} \right)^2 \quad (3)$$

where, N is the number of total observations, r_{cal_i} and $r_{\exp_i}$ are calculated from the model equation and experimental rates at the different reaction temperatures.

The rate constants and the equilibrium constants can be related to The Arrhenius equation and van't Hoff laws as shown below:

$$k_i(T) = A \exp\left(-\frac{E_{ai}}{RT}\right) \quad (4)$$

$$K_i(T) = K \exp\left(-\frac{\Delta H_i}{RT}\right) \quad (5)$$

where k_i and K_i are reaction and equilibrium constants, respectively. E_{ai} and ΔH_i are the apparent activation energy and standard enthalpy change of i species.

2.3. Effect of Space Velocity on CO Conversion

The influence of the weight hourly space velocity (WHSV) on the CO conversion for three different catalysts at 1 atm and H_2/CO molar ratio 2 with error bar is shown in Figure 7a–c. The reactions were carried out at three different temperatures (210 °C, 240 °C, and 270 °C). CO conversion increases with the increase of space velocity and temperature. While CO conversion increases quickly with the increase of space velocity at the beginning, it remains almost constant at higher space velocity as the reaction reaches the equilibrium state. The variation of CO conversion was within 10% as observed during these reactions.

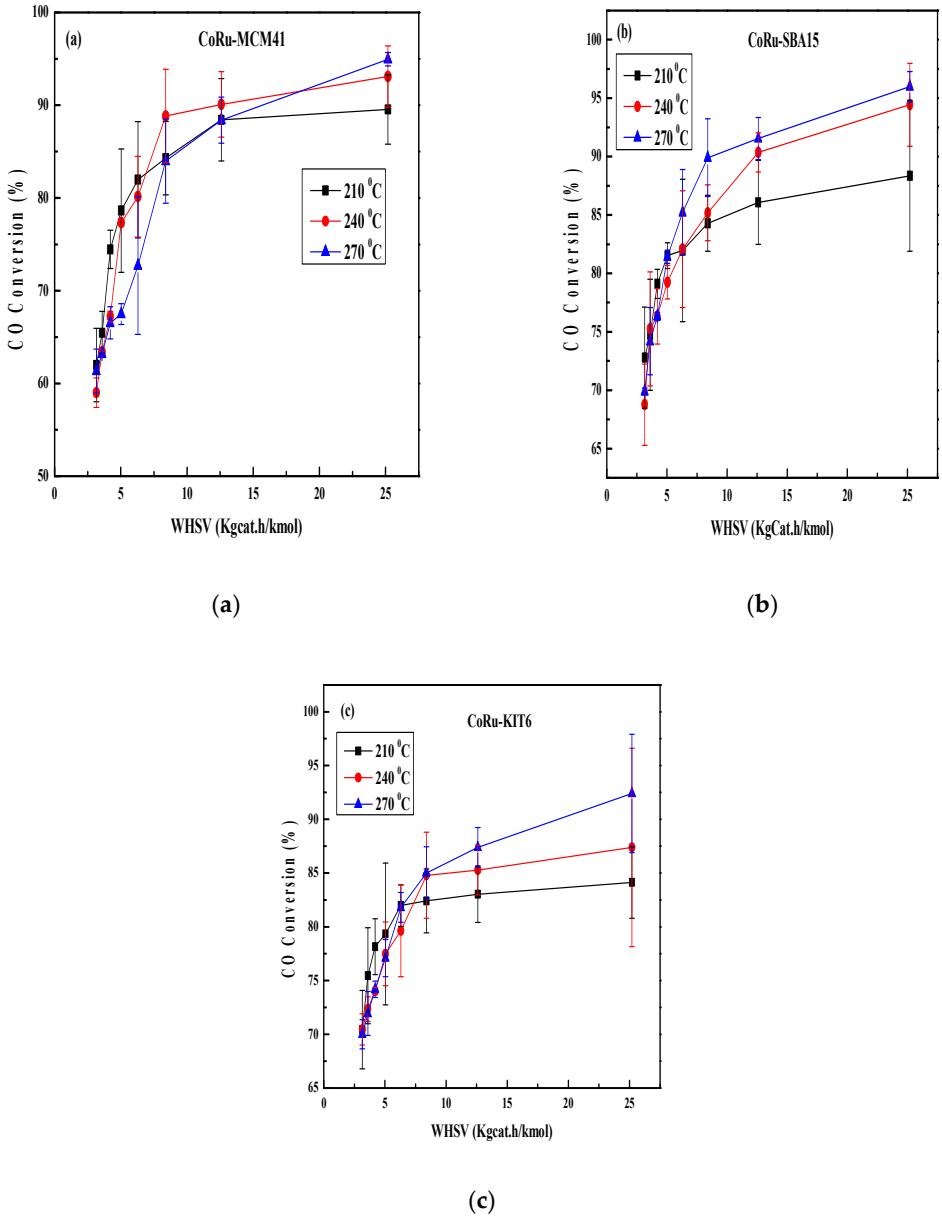

Figure 7. Effect of space velocity on CO conversion: (**a**) CoRu-MCM-41; (**b**) CoRu-SBA-15; (**c**) CoRu-KIT-6.

2.4. FT Kinetic Model

The kinetic models derived from Langmuir–Hinshelwood and Eley–Rideal mechanisms consider elementary reactions consuming CO and H_2 to produce hydrocarbons and water. Recently, the mechanistic aspects of FT synthesis were well investigated by computational catalysis studies

using DFT-based quantum chemical models [85–87]. However, the use of Langmuir–Hinshelwood and Eley–Rideal models facilitates understanding of the FT mechanism more easily. In this work, all the kinetic models derived based on these mechanisms are investigated and fitted with experimental data to check the feasibility of the proposed mechanism. The objective function (F) in Equation (4) was utilized to measure the goodness of the model to select the best-fitted mechanism for FT synthesis. Table 4 shows the experimental data obtained for all catalysts at 210 °C, 240 °C, and 270 °C.

Table 4. Kinetic experimental data for all the catalysts.

Temperature	W/F (Kgcat.h/kmol)	CoRu-MCM-41		CoRu-SBA-15		CoRu-KIT-6	
		Reaction Rate (Kmol/Kg.h)	Conversion (%)	Reaction Rate (Kmol/Kg.h)	Conversion (%)	Reaction Rate (Kmol/Kg.h)	Conversion (%)
210 °C	25.2	0.035	89.53	0.035	88.35	0.033	84.12
	12.6	0.070	88.43	0.068	86.08	0.065	83.03
	8.39	0.100	84.29	0.1	84.29	0.098	82.41
	6.30	0.130	81.97	0.13	81.97	0.13	81.97
	5.04	0.156	78.64	0.162	81.52	0.158	79.34
	4.20	0.177	74.45	0.188	79.11	0.186	78.15
	3.60	0.181	65.46	0.208	74.74	0.21	75.45
	3.15	0.196	61.98	0.231	72.79	0.224	70.43
240 °C	25.2	0.036	93.09	0.037	94.43	0.034	87.39
	12.6	0.071	90.09	0.071	90.36	0.067	85.27
	8.39	0.105	88.84	0.01	85.18	0.101	84.79
	6.30	0.127	80.14	0.013	82.07	0.126	79.63
	5.04	0.153	77.34	0.157	79.24	0.154	77.48
	4.20	0.160	67.23	0.182	76.32	0.176	74.02
	3.60	0.176	63.42	0.209	75.25	0.201	72.35
	3.15	0.187	59.02	0.218	68.76	0.224	70.44
270 °C	25.2	0.037	94.95	0.038	95.98	0.036	92.40
	12.6	0.070	88.39	0.072	91.55	0.069	87.39
	8.39	0.100	83.96	0.107	89.90	0.101	85.01
	6.30	0.115	72.70	0.135	85.22	0.130	81.80
	5.04	0.133	67.48	0.162	81.42	0.153	77.08
	4.20	0.158	66.53	0.182	76.32	0.177	74.18
	3.60	0.175	63.20	0.206	74.19	0.2	71.93
	3.15	0.194	61.34	0.222	69.90	0.222	70.00

The kinetic parameters obtained for all the mechanisms for CoRu-MCM-41 are shown in Table 5. It can be inferred from data that the value of the rate constant (*k*) increases with increasing temperature with only one of the 6 mechanisms which is FT-3. Therefore, for CoRu-MCM-41, the model FT-3 is best fitted with the kinetic data.

Table 5. Kinetic parameters obtained from proposed mechanisms for CoRu-MCM-41

Model	Temperature					
	210 °C	R^2	240 °C	R^2	270 °C	R^2
FT-1	k = 0.872 ± 0.0037 K_1 = 21.19 ± 1.79	0.88	k = 0.23 ± 0.027 K_1 = 16.49 ± 7.66	0.98	k = 0.38 ± 0.118 K_1 = 3.92 ± 2.46	0.98
FT-2	k = 0.87 ± 0.0037 K_1 = 21.19 ± 1.79	0.88	k = 0.74 ± 0.0014 K_1 = 21.19 ± 0.84	0.72	k = 0.69 ± 0.0067 K_1 = 6.05 ± 0.34	0.93
FT-3	**k = 1.32 ± 0.000029 K_1 = 5.04 ± 0.000194 K_2 = 2.877 ± 0.000468**	**0.97**	**k = 2.21 ± 0.017 K_1 = 4.02 ± 0.103 K_2 = 0.51 ± 0.0064**	**0.96**	**k = 3.22 ± 0.068 K_1 = 1.41 ± 0.05 K_2 = 0.5 ± 0.019**	**0.97**
FT-4	k = 0.443 ± 1.69 K_1 = 1.88 ± 19.53 K_2 = 2.49 ± 34.08	0.98	k = 0.85 ± 0.015 K_1 = 11.09 ± 0.686 K_2 = 0.365 ± 0.0077	0.98	k = 2.01 ± 0.037 K_1 = 3.13 ± 0.11 K_2 = 0.228 ± 0.0045	0.98

FT-5	k = 0.536 ± 0.000355 K_1 = 21.19 ± 0.403 K_2 = 2.42 ± 0.0023	0.97	k = 0.48 ± 0.000205 K_1 = 21.19 ± 0.265 K_2 = 2.33 ± 0.0015	0.90	k = 0.41 ± 0.009 K_1 = 0.33 ± 0.014 K_2 = 11.09 ± 0.396	0.97
FT-6	k = 0.704 ± 0.0022 K_1 = 0.931 ± 0.0039 K_2 = 31.29 ± 3.21 K_3 = 1.77 ± 0.0074	0.96	k = 0.67 ± 0.0012 K_1 = 0.897 ± 0.0021 K_2 = 31.29 ± 1.83 K_3 = 1.69 ± 0.0041	0.87	k = 0.243 ± 0.00018 K_1 = 3.14 ± 0.0052 K_2 = 31.29 ± 0.76 K_3 = 1.67 ± 0.0027	0.83

In order to determine the activation energy and the frequency factor from the Arrhenius equation, the logarithm of the rate constant was plotted against the inverse of reaction temperature as shown in Figure 8. The activation energy was determined to be 32.21 kJ/mol and the frequency factor was 4099 kmol/KgCat.hr. $(atm)^2$ for CoRu-MCM-41 catalyst. Table 6 shows that the rate constant increases with the increase of reaction temperature. However, the two adsorption equilibrium constants (K_1 and K_2) decrease with the increase of reaction temperature. Since adsorption is an exothermic process, the adsorption equilibrium constant decreases with rise in temperature.

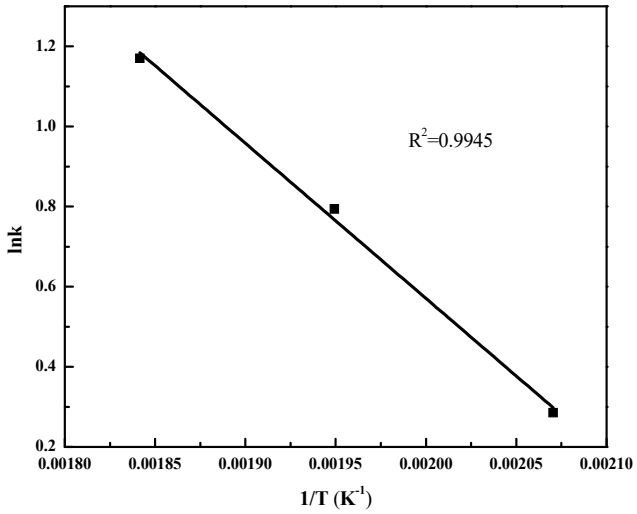

Figure 8. Arrhenius plot-based on Langmuir–Hinselwood (LH) model for FT synthesis over CoRu-MCM-41 catalyst.

Table 4 shows the experimental data of the kinetic runs for CoRu-SBA-15 at 210 °C, 240°C, and 270 °C. When the data are fit against all the kinetic models, FT-2 was the best-fitted model obtained for CoRu-SBA-15. The kinetic parameters for all of the proposed mechanisms are shown in Table 6.

Table 6. Kinetic parameters obtained from proposed mechanisms for CoRu-SBA-15.

Model	**Temperature**					
	210 °C	**R^2**	**240 °C**	**R^2**	**270 °C**	**R^2**
FT-1	k = 3.02 ± 0.092 K_1 = 0.46 ± 0.015	0.94	k = 2.01 ± 0.059 K_1 = 0.655 ± 0.021	0.94	k = 2.01 ± 0.026 K_1 = 0.727 ± 0.01	0.98
FT-2	**k = 9.08 ± 0.266** **K_1 = 0.166 ± 0.005**	**0.94**	**k = 11.09 ± 0.281** **K_1 = 0.118 ± 0.0033**	**0.95**	**k = 13.12 ± 0.005** **K_1 = 0.109 ± 0.000046**	**0.99**
FT-3	k = 11.09 ± 0.698 K_1 = 2.23 ± 0.145 K_2 = 20.62 ± 1.49	0.82	k = 2.01 ± 0.043 K_1 = 10.79 ± 0.285 K_2 = 17.51 ± 0.536	0.79	k = 11.09 ± 0.337 K_1 = 2.01 ± 0.063 K_2 = 18.10 ± 0.645	0.95

FT-4	k = 11.09 ± 0.379 K_1 = 0.161 ± 0.0057 K_2 = 0.761 ± 0.026	0.94	k = 2.01 ± 0.0026 K_1 = 0.283 ± 0.00042 K_2 = 2.31 ± 0.0032	0.93	k = 2.01 ± 0.037 K_1 = 3.13 ± 0.11 K_2 = 0.228 ± 0.0045	0.98
FT-5	k = 2.01 ± 0.026 K_1 = 0.189 ± 0.0031 K_2 = 4.41 ± 0.062	0.92	k = 2.01 ± 0.0237 K_1 = 0.193 ± 0.0029 K_2 = 3.92 ± 0.050	0.94	k = 2.01 ± 0.032 K_1 = 0.205 ± 0.0036 K_2 = 3.62 ± 0.063	0.98
FT-6	k = 2.01 ± 0.037 K_1 = 0.988 ± 0.021 K_2 = 0.894 ± 0.031 K_3 = 1.57 ± 0.032	0.90	k = 6.05 ± 0.253 K_1 = 0.273 ± 0.012 K_2 = 0.266 ± 0.014 K_3 = 3.56 ± 0.153	0.94	k = 2.01 ± 0.018 K_1 = 0.937 ± 0.0094 K_2 = 2.18 ± 0.057 K_3 = 1.09 ± 0.011	0.97

The activation energy and frequency factor of this catalyst were evaluated from the Arrhenius equation by plotting the logarithm of the rate constant to the inverse of reaction temperature as shown in Figure 9. The activation energy was determined to be 13.39 kJ/mol and the frequency factor was 254 kmol/KgCat.hr. atm. Table 6 shows that for FT-3 mechanism, the reaction rate constant increases with reaction temperature and adsorption equilibrium constant (K_1) decreases with the increase of reaction temperature.

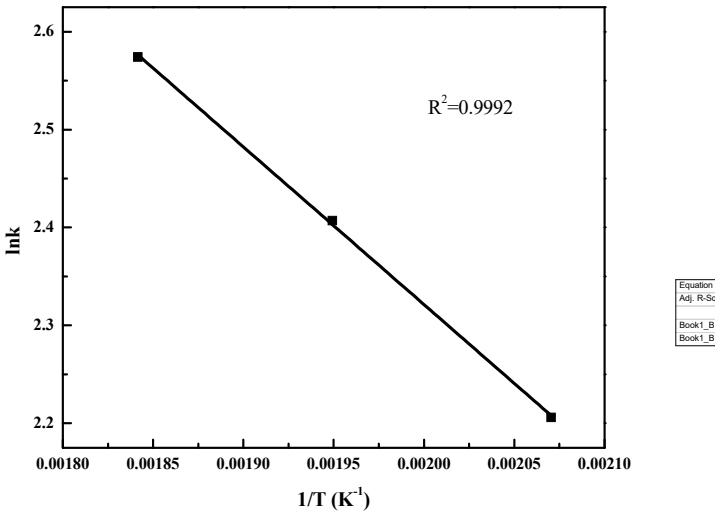

Figure 9. Arrhenius plot-based on LH model for FT synthesis over CoRu-SBA-15 catalyst.

Table 4 shows the experimental data for CoRu-KIT-6 catalyst. All the models were fitted with this experimental kinetic data and FT-6 was found to be the best fitted model for CoRu-KIT-6. The kinetic parameters for all the proposed mechanisms are shown in Table 7 and the activation energy from Figure 10 was determined to be 12.59 kJ/mol and the frequency factor was 39 kmol/KgCat.hr. atm.

Table 7. Kinetic parameters obtained from all the proposed mechanisms for CoRu-KIT-6.

Model	**Temperature**					
	210 °C	**R²**	**240 °C**	**R²**	**270 °C**	**R²**
FT-1	k = 2.18 ± 8.89 K_1 = 0.73 ± 3.28	0.97	k = 0.79 ± 0.543 K_1 = 2.13 ± 1.91	0.98	k = 1.38 ± 1.42 K_1 = 1.19 ± 1.44	0.99
FT-2	k = 1.42 ± 0.00044 K_1 = 11.09±0.038	0.95	k = 1.29±0.022 K_1 = 11.09±2.09	0.98	k = 2.02±3.30 K_1 = 1.94±8.71	0.98

FT-3	k = 11.09±0.316 K_1 = 0.892±0.031 K_2 = 0.279±0.013	0.96	k = 10.09±0.166 K_1 = 0.882±0.018 K_2 = 0.279±0.0073	0.98	k = 11.09±0.088 K_1 = 1.94±0.016 K_2 = 15.64±0.15	0.97
FT-4	k = 2.01±0.052 K_1 = 0.122±0.0038 K_2 = 7.27±0.203	0.97	k = 2.01±0.088 K_1 = 1.195±0.067 K_2 = 0.694±0.033	0.98	k = 2.01±0.072 K_1 = 0.355±0.015 K_2 = 2.29±0.089	0.99
FT-5	k = 2.01±0.051 K_1 = 0.121±0.0038 K_2 = 7.27±0.203	0.97	k = 1.46±0.00069 K_1 = 10.08±0.055 K_2 = 0.91±0.00049	0.92	k = 2.01±0.028 K_1 = 0.842±0.022 K_2 = 1.62±0.024	0.99
FT-6	**k = 1.71±0.02** **K_1 = 1.39±0.02** **K_2 = 0.828±0.018** **K_3 = 1.61±0.021**	**0.95**	**k = 2.01±0.039** **K_1 = 1.11±0.027** **K_2 = 0.454±0.013** **K_3 = 2.21±0.048**	**0.98**	**k = 2.41±0.040** **K_1 = 0.91±0.017** **K_2 = 0.315±0.0071** **K_3 = 3.12±0.056**	**0.99**

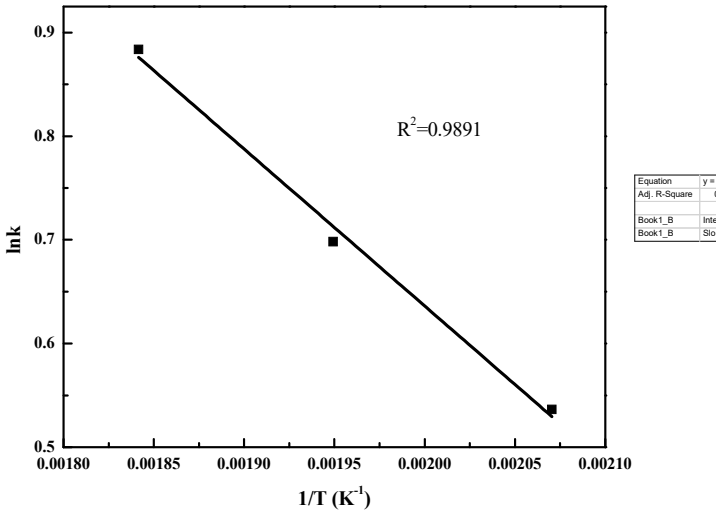

Figure 10. Arrhenius plot-based on LH model for FT synthesis over CoRu-KIT-6 catalyst.

Based on our experimental and kinetic model data, it can be concluded that only one of the six mechanisms for each catalyst is statistically relevant for fitting the model. The rate constant (*k*), for some of the other five mechanisms, does not show an increasing trend with the increase in temperature or remains constant, while the equilibrium constants, K_1 and K_2, did not show the decreasing trend with the increase in temperature. Thus, FT-3, FT-2, and FT-6 mechanisms were considered as kinetically relevant model equations for CoRu-MCM-41, CoRu-SBA-15, and CoRu-KIT-6, respectively.

The results from our studies in a microreactor are similar to those reported in literature. Mansouri et al., developed a similar mechanism to estimate kinetic parameters for FT synthesis using cobalt-based catalyst with silica support and found that the experimental data were best fitted with surface reaction mechanism proposed based on Langmuir-Hineshelwood model and the optimal activation for the proposed kinetic model was found to be 31.57 kJ/mol [88]. Very recently, Sonal et al., detailed mechanistic approach for FT synthesis based on Langmuir–Hinshelwood–Hougen–Watson (LHHW) and Eley–Rideal using Fe–Co based catalyst. They claimed that a mechanism based on the adsorption and desorption have a satisfactory fit to the experimental data with the activation energies for the formation of methane, paraffin and olefin to be around 70 kJ/mol, 113 kJ/mol, and 91

kJ/mol, respectively [89]. In order to improve the efficiency of FT synthesis significantly, detailed kinetic rate expressions were derived which is very similar to our work reported in literature for both fixed bed reactor as well as microreactor using iron or cobalt-based catalyst [80,81,90,91]. The elementary steps in the above studies were used to develop kinetic mechanisms considering FT reactions with and without water gas shift (WHS) reactions occurring on the surface of the catalysts forming intermediates with active sites. A similar approach was considered in this present study where CO*, COH_2* are assumed to form as intermediates, where * is an active site of the catalyst. From the activation energy calculations, shown in Figures 8–10, the FT activation energy is observed in the order, CoRu-MCM-41 > CoRu-SBA-15 > CoRu-KIT-6. Almost 20 kJ/mol less activation energy was obtained for SBA-15 supported catalyst than that of MCM-41 catalyst. The activation energy of KIT-6 supported catalyst is a bit less than that of SBA-15 supported catalyst. This reflects that activation energy depends on metal–support interactions in different mesoporous catalysts. The variation of activity in different mesoporous catalysts might arise due to experimental uncertainties and operating conditions [92]. In addition, the FT activation energy is sensitive to the reactor system. Sun et al., [93] reported that the activation energy in a microchannel microreactor is smaller than that observed in a fixed bed reactor (FBR).

Figure 11 shows the variation of the model predicted rate with the experimental rate for all catalysts. The best fitted models i.e., FT-3, FT-2, and FT-6 for CoRu-MCM-41, CoRu-SBA-15, CoRu-KIT-6, respectively, were chosen to plot the graph for predicted and experimental rates. The correlation coefficient (R^2) for all cases was above or equal to 0.95 with an error band of ±15% to ±30%. This indicates that the error between experimental and predicted values lies within the statistical permissible limits at all reaction temperatures for all the catalysts and consistent with the mechanistic models proposed in the literature. Moazami et al., conducted kinetic studies for FT synthesis in a fixed bed reactor with cobalt-based catalyst over silica support and found that 60% of the results were predicted with a relative error of less than 15%, while the rest of the proposed kinetic models has error less than 32% with confidence interval of 0.99 [94]. They also proposed a pseudo-homogenous one-dimensional model to evaluate the kinetic performance of the catalyst and achieved less than 8% error with the predicted data for kinetic experiments [95]. More recently, Marchese et al., performed kinetic studies with Co-Pt/γ-Al_2O_3 catalyst in a lab-scale tubular reactor and reported an error band around ± 25% with a confidence level of 0.95 stating it lies in the suitable acceptable limits with many mechanistic models proposed in the literature [89,96–98].

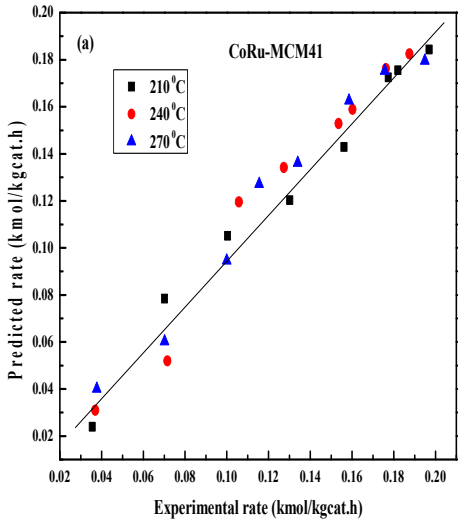

(**a**)

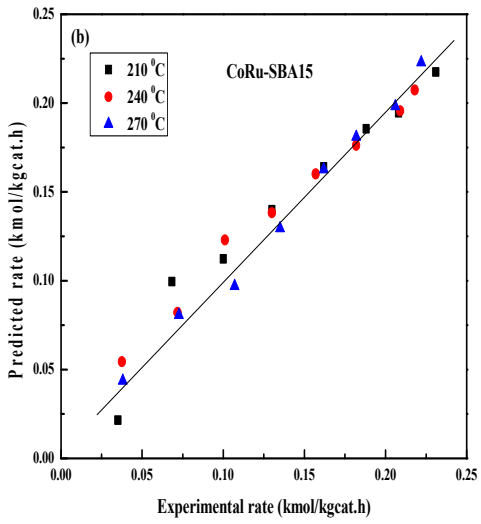

(**b**)

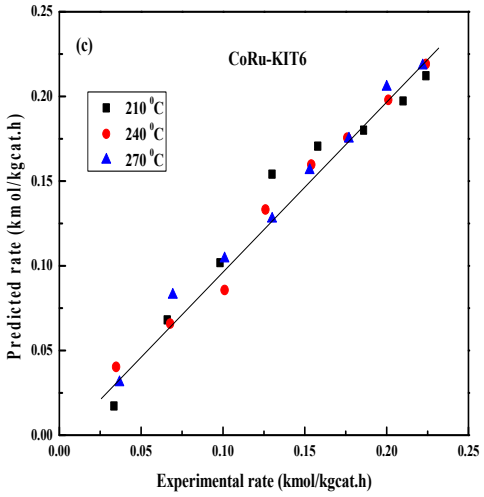

(**c**)

Figure 11. Experimental rate vs predicted rate for all temperature of three different catalysts: (**a**) CoRu-MCM-41; (**b**) CoRu-SBA-15; (**c**) CoRu-KIT-6.

2.5. Deactivation Studies

In order to further understand how the interaction of Co and Ru metals with different mesoporous silica supports affects the stability of the FT catalysts, deactivation studies were performed. Figure 12 shows the deactivation rates of the catalysts tested continuously for 60 h at 240 °C, 1 atm, and H_2:CO ratio of 2:1. All the catalysts maintained fairly consistent CO conversion with very little fluctuation during the first 10 h. More specifically, the catalysts maintained 65%–79% CO conversion in the first 10 h of the reaction with CoRu-KIT-6 exhibiting the highest conversion and CoRu-MCM-41, the lowest. The activity of all the catalysts dropped by 20% after 24 h and then started to decline further. At the end of 60 h, the activity of the CoRu-MCM-41 dropped by 70% whereas, in the case of CoRu-KIT-6 and CoRu-SBA-15, the CO conversion decreased by 64% and 84%, respectively. Our results suggest that in terms of stability, the support has a significant impact on FT performance. More significantly, MCM-41 and KIT-6 supports are more stable when compared to the FT stability studies with SBA-15.

Many deactivation mechanisms have been proposed for FT studies that include catalysts poisoning, sintering, oxidation, the effect of water, carbon deposition and surface reconstruction [99]. The syngas used in our studies is a mixture of ultrahigh pure 5.0 CO and H_2 gases; therefore, there is very little or no chance of catalyst deactivation due to poisoning by the gas feed at the inlet to the reactor. It was also observed in our previous studies that the support (SiO_2 vs TiO_2) can enhance the stability of the catalyst to resist deactivation [38,40]. Iglesia et al., noticed that silica supported materials are less stable when compared to the other supports like Al_2O_3 [100] in their FT studies with Co-based catalyst. They also reported that CoRu-TiO_2 and CoRu-SiO_2 were found to have almost the same activation energy upon the addition of Ru to the Co catalyst; however, there were strong differences in the deactivation rates of catalysts depending upon the support [101]. Based on our CO-conversion studies, the ability of catalysts to withstand or retard the FT deactivation rate was in the order of CoRu-KIT-6 > CoRu-MCM-41 > CoRu-SBA-15.

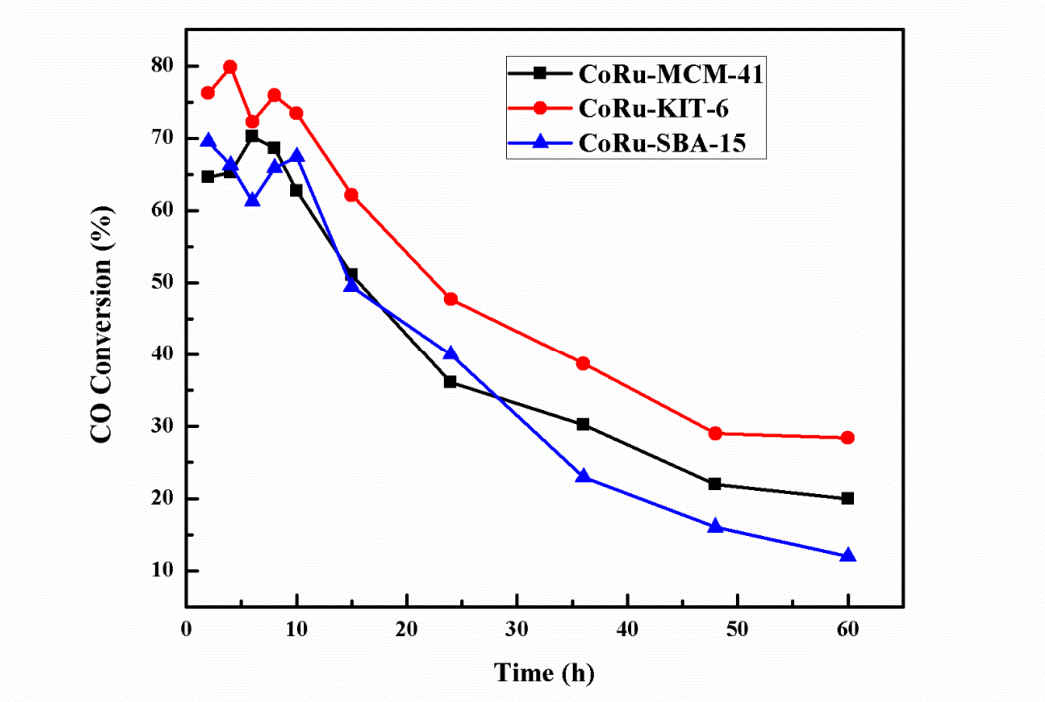

Figure 12. Deactivation studies of the catalysts at T = 240 °C, P = 1 atm and H_2:CO = 2:1.

3. Materials and Methods

3.1. Materials

The reagents used for catalysis synthesis were of analytical grade with no further purification. Tetramethyl orthosilicate, 99% (TMOS) and ammonium hydroxide, Tetraethyl orthosilicate reagent grade, 98% (TEOS), Pluronic acid (P123), Hydrochloric acid (HCl), Cetyltrimethylammoniumbromide (CTAB), $Co(NO_3)_2.6H_2O$, $RuCl_3{\cdot}xH_2O$ were purchased from Sigma Aldrich. Ethanol (anhydrous), Butanol and acetone, ACS grade, were obtained from Fischer Scientific, Branchburg, New Jersey, USA.

3.2. Fabrication of Microreactor

The microchannel microreactor and the respective cover channel were fabricated using 3D printing technology. Typically, the microreactor and its cover channel are designed using AutoCAD software which is schematically shown in Figure 13. The design is based on the split and recombination principle which has 11 microchannels of 500 μm × 500 μm × 2.4 cm as reaction zone in between them. This stainless-steel 3D printed microreactor is assembled in a custom-built heating block with an inlet and outlet system which facilitates the flow of syngas through the channels.

3.3. Catalyst Synthesis and Loading

Three types of Co-Ru based nanocatalysts supported by different mesoporous silica supports i.e., MCM-41, SBA-15 and KIT-6 supports are used in this study. A constant metal loading of 10%Co and ~5% Ru in weight was maintained in all preparations and this metal loading was also determined using the amount of the precursor. Three catalysts using different mesoporous support—10%Co5%Ru-MCM-41, 10%Co5%Ru-SBA-15 and 10%Co5%Ru-KIT-6—were synthesized using the one-pot hydrothermal procedure (as shown below) [48]. The catalysts were labeled as CoRu-MCM-41, CoRu-SBA-15, and CoRu-KIT-6 in this manuscript.

For the synthesis of CoRu-MCM-41, TMOS, CTAB, DI-water, and ethanol were used in a molar ratio of 1:0.13:130:20 as described elsewhere [48]. In short, CTAB was dissolved in DI-water at 30 °C to produce a clear solution. The metal precursors were dissolved in ethanol in a separate beaker. The precursor, TMOS, which is a limiting agent for this synthesis, was added dropwise to the mixture of the two solutions prepared previously. Ammonium hydroxide was added dropwise to precipitate metal hydroxides in the solution, till the final pH was ~10. The precipitate was stirred for 3 h, followed by 18 h of aging at 65 °C. The precipitate was then washed with DI water till the filtrate reached a pH of 7, finally washed with ethanol and filtered. The filtered material is air-dried for a day and then oven-dried at 110 °C for 24 h. The dried catalyst is calcined at 550 °C for 16 h with a ramp rate of 2 °C/min to remove the CTAB template.

For the synthesis of CoRu-SBA-15: TEOS, CTAB, water, ethanol, pluronic acid, and hydrochloric acid were mixed in molar ratios of 1:0.081:41:7.5:0.0168:5.981. In a typical synthesis procedure, P123 was dissolved in 2M HCl at 35 °C till a clear solution was obtained. Another solution was prepared by dissolving CTAB in DI water at 35 °C until a homogenous mixture was produced. These two solutions were mixed and stirred for 35 min. Ethanol containing metal precursors were added dropwise into the solution and stirred for 30 min. Afterwards, TEOS which was limiting reagent in this procedure was also added dropwise and stirred for 20 h at 35 °C. The aqueous solution was aged for 48 h at 98 °C followed by air drying for 24 h. The material was then oven-dried at 110 °C for 24 h. Finally, the dried material is then calcined in stepwise fashion with heating rate of 1 °C/min at 350 °C, 450 °C, and 550 °C for 8 h each, respectively to remove CTAB and pluronic acid.

In the case of CoRu-KIT-6, TEOS, P123, HCl, DI water, and butanol were mixed in a molar ratio of 1:0.017:1.83:195:1.31 [102]. For a typical procedure, P123 was added to HCl at 35 °C till a clear solution was obtained. A separate solution was prepared with butanol containing metal precursors and poured to the previous solution and stirred until a homogeneous solution was obtained. To this mixture, TEOS, which was the limiting reagent, was added dropwise and stirred at 500 rpm for 24 h. The final solution was aged for 24 h at 100 °C, followed by air drying for 24 h under the fume hood. The material is oven-dried at 110 °C for 24 h and then calcined at 550 °C for 4 h, to remove P123, the structure directing agent, SDA, with heating and cooling rates of 1 °C/min.

The catalyst is loaded into the microchannels of the microreactor using a PVA suspension containing the catalyst, DI water, binder PVA (polyvinyl alcohol 98%–99% hydrolyzed MW: 31000) and acetic acid of weight ratio 1:5:0.25:0.05. This suspension with well-dispersed catalyst was dip-coated and dried in air and then calcined in presence of air at 400 °C for 2 h with heating and cooling rates of 5 °C/min. Figure 13d shows the SEM image of the catalyst coated microreactor prior to the in-situ reduction.

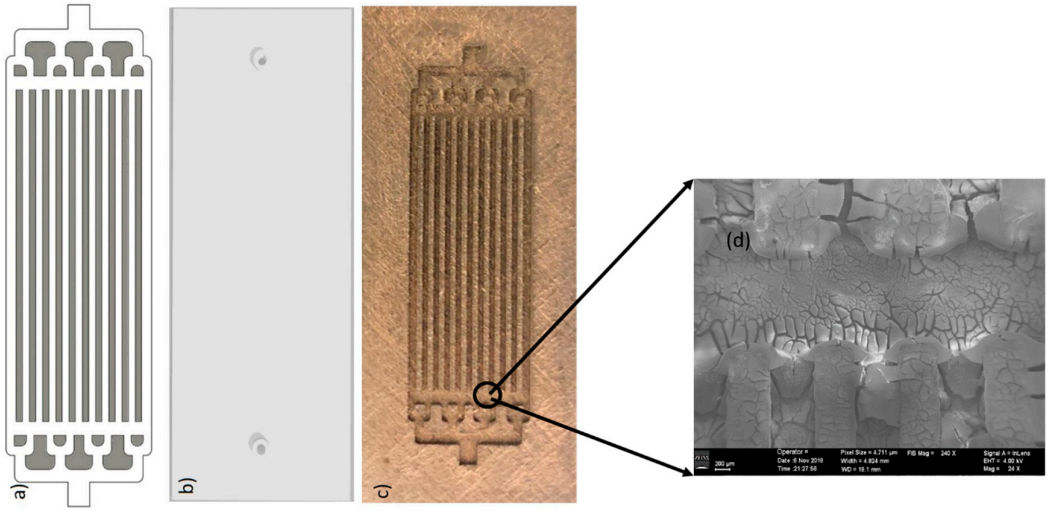

Figure 13. (**a**) and (**b**): AutoCAD design of the microreactor and cover channel (**c**) 3D printed reactor, (**d**) SEM image of the microchannels coated with catalyst prior to FT studies.

3.4. Catalyst Characterization

Specific surface area, pore size, pore volume and TPR studies of the catalyst were carried out using Micromeritics, 3-Flex instrument. The Brunner–Emmett–Teller (BET) method was used to calculate the surface area of the catalyst where an equation was obtained from adsorption isotherm in the relative pressure range of 0.07–0.03. The surface area was calculated from adsorption isotherm in the relative pressure range of P/P_0 = 0.07–0.3 using the Brunner–Emmett–Teller (BET) equation. The total volume per gram of catalyst was determined from the amount of N_2 adsorbed at P/P_0 = 1. The N_2 desorption from the catalyst surface provides information about the pore size distribution using BJH (Barret–Joyner–Halenda) plots [103]. The H_2 temperature programmed reduction (TPR) analysis was also done with the same instrument which has a TCD detector to monitor the reduction signals of the catalyst. Around 50 mg of the catalyst was loaded into the quartz sample tube in which a stream of 10% H_2/Ar at flowrate 110 mL/min was passed through and the temperature is increased to 1000 °C with 10 °C/min ramp rate. The small and wide-angle powder x-ray diffraction (XRD) were recorded using D8 Discover X-ray and Rigaku SmartLab X-ray diffractometers, respectively, with Cu K-alpha radiation (wavelength = 0.15418 nm) radiation generated at 40 mA and 40 kV. The step size and time per step used in these measurements are 0.05° and 3 secs/step, respectively. The crystal sizes of the metal oxides were determined using the Scherrer equation. In the Scherrer equation below, τ stands for the crystal size, λ is the wavelength of the Cu Kα radiation, β is the full width half maximum and θ is the Bragg diffraction angle.

$$\tau = \frac{0.9\lambda}{\beta * \mathrm{Cos}\theta} \quad (6)$$

The morphology and the size of the catalysts were analyzed using transmission electron (TEM Carl Zeiss Libra 120) at 120 KeV and scanning electron microscopy (Zeiss Auriga FIB/FESEM). The sample for TEM was prepared by dispersing a small quantity of catalyst in 3 mL of ethanol followed by vortex dispersion and sonication for a few minutes. Then the suspension was drop coated on a carbon-coated copper grid of 300 μm mesh size, followed by drying in an oven at 100 °C for 12 h.

The elemental composition and oxidation states of the metals were analyzed using Energy Dispersive X-ray spectrometry (Zeiss Auriga FIB/FESEM obtained from Carl Zeiss, Oberkochen, Germany) and oxidation states by X-ray photoelectron spectroscopy (XPS-Escalab Xi+-Thermo Scientific obtained from Thermo Scientific, West Sussex, UK), respectively.

3.5. Fischer–Tropsch Synthesis in Microreactor and Kinetic Data Collection

An in-house LabVIEW automated experimental setup was built to carry out the FT experiments for precise control over the operating conditions. The experimental setup is shown in Figure 14. The flowrates of the syngas mixture which is a mixture of hydrogen and carbon monoxide were controlled by precalibrated mass flow controllers obtained from cole parmer with flow rates ranging from 0–1 sccm. Nitrogen was used as a carrier gas into the system and was controlled by Aalborg mass flow controller with a maximum flow rate of 10 sccm. The upstream and downstream pressures were continuously monitored by pressure gauges obtained from Cole–Parmer and the data are fed to Aalborg solenoid valve from which the reaction pressure is controlled and kept constant throughout the reaction. All these controllers are operated by LabVIEW 2018 program. The product stream is directly fed to the GC-MS (Agilent Technologies 7890B GC and 5977 MSD). Prior to the start of the kinetic experiments, the microreactors were reduced ex-situ in Carbolite Gero tubular furnace with 10% H_2Ar. To compensate the losses while transferring the microreactor to the heating block the microreactor containing the catalyst was reduced again in-situ for 6 h at 350 °C before the start of FT reaction. The kinetic studies were performed by varying the weight hourly space velocity (WHSV = $W_{cat}/F_{CO,in}$, where W_{Cat} = weight of the catalyst and $F_{CO,in}$ = molar flow rate of CO in feed) in the range of ~25.2–3.15 kgcat.h/kmol. The reactions were performed with syngas having a feed molar ratio (H_2/CO) of 2:1 at 210 °C, 240 °C, and 270 °C while the reaction pressure was maintained at 1 atm. Based on our previous FT studies using this setup and preliminary runs, all reactions reached a steady state after an hour at each setpoint of WHSV. Deactivation studies were also performed for all three

catalysts at 240 °C using syngas feed molar ration of 2:1. CO conversion was calculated based on following equation:

$$X_{CO}\% = \frac{F_{CO,in} - F_{CO,out}}{F_{CO,in}} \times 100 \quad (7)$$

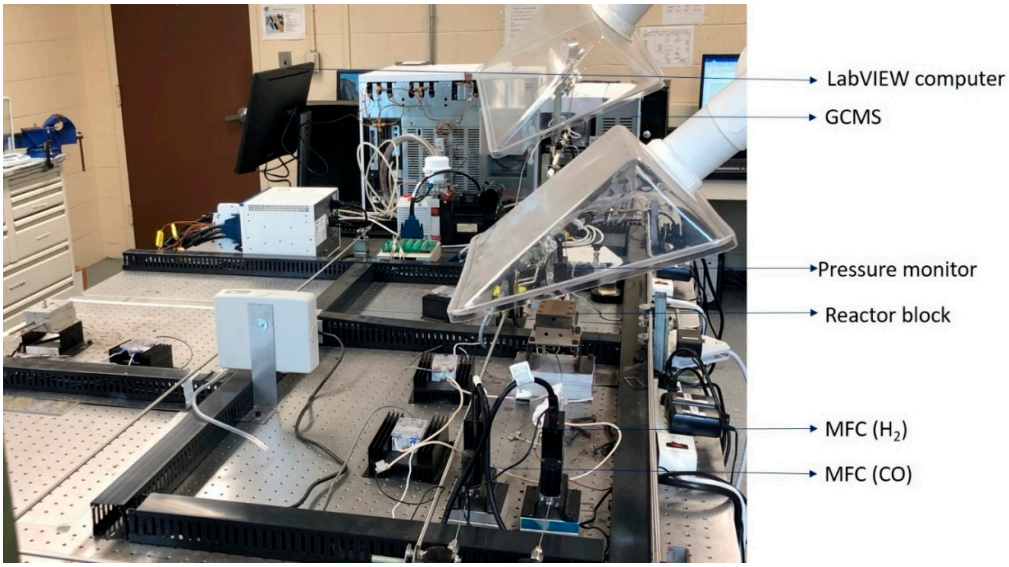

Figure 14. Experimental set-up for FT synthesis in a 3-D printed stainless steel microreactor.

4. Conclusions

Three different types of mesoporous silica supported Co-Ru based catalysts were synthesized using the one-pot hydrothermal method and performance for FT was evaluated. These catalysts resulted in high surface area with hexagonal ordered mesoporous structure as supported by BET, low angle XRD and TEM studies. The interaction between the metal and different types of support has a significant effect on the kinetic and stability studies of FT synthesis. Six mechanistic models were developed based on the Langmuir–Hinshelwood and Eley-Radiel mechanisms. The best fitted model for all catalysts was obtained on the basis of non-linear regression by comparing with the objective function which is equation-7 in this paper. The proposed model FT-3 was best fitted with the kinetic data for CoRu-MCM-41 catalyst. Whereas, FT-2 and FT-6 were well fitted with the kinetic data for CoRu-SBA-15 and CoRu-KIT-6, respectively. CoRu-KIT-6 was found to be more active than other catalysts with a low activation energy of 12.59 kJ/mol, whereas for CoRu-SBA-15 and CoRu-MCM-41 the activation energies are 13.39 and 32.21 kJ/mol, respectively. An average error of 5.65%, 1.76%, and 3.70% was obtained for catalysts CoRu-MCM-41, CoRu-SBA-15, CoRu-KIT-6, respectively considering the best fitted model explained above for FT synthesis. The predicted data provided by kinetic models were satisfactory with the experimental data. These results highlight the potential of the mechanistic FT models as well as reaction mechanisms to further improve the performance of FT synthesis. In addition, this information can help to design more active and selective catalysts for the optimized FT process. Furthermore, all catalysts exhibited significant resistance to the deactivation rate following the order CoRu-KIT-6> CoRu-MCM-41>CoRu-SBA-15. This study suggests that even if the support is of same type, the structure of the support plays a vital role in catalyst performance for FT synthesis.

Supplementary Materials: The following are available online at www.mdpi.com/xxx/s1, Figure S1: title, Table S1: title.

Author Contributions: Methodology, analysis and experimental investigation by N.M. and S.B.; project administration and supervision by S.A., and D.K.; all the authors contributed to the discussion of the experimental results as well as writing and editing of the manuscript.

Funding: This project received funding from NSF CREST (#260326) and UNC-ROI (#110092). This work is performed at North Carolina A&T State University and Joint School of Nanoscience and Nanoengineering, a member of the Southeastern Nanotechnology Infrastructure Corridor (SENIC) and National Nanotechnology Coordinated Infrastructure (NNCI), which is supported by the National Science Foundation (Grant ECCS-1542174).

Acknowledgments: The authors gratefully acknowledge Dr.Kyle Nowlin and Mr. Klinton Davis for TEM support, and Dr. Xin Li for XRD support.

Conflicts of Interest: The authors declare no conflict of interest

Appendix A

Derivation of Kinetic model:

FT-3 kinetic model

Dual-site adsorption of CO and H_2, the surface reaction is rate controlling step (RCS)

$$CO + * \underset{k_{-1}}{\overset{k_1}{\rightleftharpoons}} CO* \quad K_1 = \frac{k_1}{k_{-1}} \text{ (Adsorption 1)} \tag{A1}$$

$$H_2 + * \underset{k_{-2}}{\overset{k_2}{\rightleftharpoons}} H_2* \quad K_2 = \frac{k_2}{k_{-2}} \text{ (Adsorption 2)} \tag{A2}$$

$$CO* + H_2* \xrightarrow{k} C + D + 2* \text{ (Surface reaction) (RCS)} \tag{A3}$$

From step 1 (Adsorption 1 (rapid reaction)),

The rate of formation of CO* is,

$$r_{CO*} = k_1 p_{CO} C_* - k_{-1} C_{CO*} \tag{A4}$$

From step 2 (Adsorption 2 (rapid reaction[89])),

The rate of formation of H_2* is,

$$r_{H_2*} = k_2 p_{H_2} C_* - k_{-2} C_{H_2*} \tag{A5}$$

From step 3 (Surface reaction 3),

$$-r_{CO} = k C_{CO*} C_{H_2*} \tag{A6}$$

According to pseudo steady-state hypothesis (PSSH), the rate of formation of the intermediate is zero.

So,

$$r_{CO*} = 0 \tag{A7}$$

$$r_{H_2*} = 0 \tag{A8}$$

So, putting the value of r_{CO*} from Equation (A4) in Equation (A7), we have,

$$\begin{aligned} & k_1 p_{CO} C_* - k_{-1} C_{CO*} = 0 \\ & \Rightarrow k_1 p_{CO} C_* = k_{-1} C_{CO*} \end{aligned} \tag{A8}$$

$$\Rightarrow C_{CO^*} = \frac{k_1 p_{CO} C_*}{k_{-1}}$$

$$\Rightarrow C_{CO^*} = K_1 p_{CO} C_*$$

So, putting the value of r_{H_2*} from Equation (A5) in Equation (A8), we have,

$$k_2 p_{H_2} C_* - k_{-2} C_{\mathrm{H_2}*} = 0$$

$$\Rightarrow k_2 p_{H_2} C_* = k_{-2} C_{\mathrm{H_2}*}$$

$$\Rightarrow C_{\mathrm{H_2}*} = \frac{k_2 p_{H_2} C_*}{k_{-2}} \quad \text{A9}$$

$$\Rightarrow C_{\mathrm{H_2}*} = K_2 p_{H_2} C_*$$

Taking the values of C_{CO^*} and $C_{\mathrm{H_2}*}$ from Equations(A9) and (A10) and putting in Equation (A6, we have,

$$-r_{CO} = kK_1K_2 p_{CO} p_{H_2} C_*^2 \quad \text{A11}$$

Making the catalyst active site balance.

Considering, the total site is,

$$C_T = 1$$

$$\Rightarrow (No.of\ vacant\ sites) + (No.of\ occupied\ sites) = 1$$

$$\Rightarrow (\mathrm{C}_*) + (\mathrm{C}_{CO^*} + \mathrm{C}_{H_2*}) = 1$$

$$\Rightarrow (\mathrm{C}_*) + (K_1 p_{CO} C_* + K_2 p_{H_2} C_*) = 1 \quad \text{A12}$$

$$\Rightarrow \mathrm{C}_*(1 + K_1 p_{CO} + K_2 p_{H_2}) = 1$$

$$\Rightarrow \mathrm{C}_* = \frac{1}{(1 + K_1 p_{CO} + K_2 p_{H_2})}$$

Putting the value of C_* from Equation (A12) in Equation (A11), we get,

$$\Rightarrow -r_{CO} = \frac{kK_1K_2 p_{CO} p_{H_2}}{(1 + K_1 p_{CO} + K_2 p_{H_2})^2} \text{ (FT-3)}$$

[Taking values of C_{CO^*} and $C_{\mathrm{H_2}*}$ from Equations (A9) and (A10)]

References

1. Fischer, F.; Tropsch, H. The synthesis of petroleum at atmospheric pressures from gasification products of coal. *Brennstoff-Chemie* **1926**, *7*, 97–104.
2. Steynberg, A.P. Chapter 1—Introduction to Fischer-Tropsch Technology. In *Studies in Surface Science and Catalysis*; Steynberg, A., Dry, M., Eds.; Elsevier: Amsterdam, The Netherlands, 2004; Volume 152, pp. 1–63.
3. Davis, B.H. Overview of reactors for liquid phase Fischer—Tropsch synthesis. *Catal. Today* **2002**, *71*, 249–300, doi:10.1016/S0920-5861(01)00455-2.
4. Wood, D.A.; Nwaoha, C.; Towler, B.F. Gas-to-liquids (GTL): A review of an industry offering several routes for monetizing natural gas. *J. Nat. Gas Sci. Eng.* **2012**, *9*, 196–208.
5. Pohar, A. Process Intensification through Microreactor Application. *Chem. Biochem. Eng. Q.* **2009**, *23*, 537–544.

6. Lerou, J.J.; Tonkovich, A.L.; Silva, L.; Perry, S.; McDaniel, J. Microchannel reactor architecture enables greener processes. *Chem. Eng. Sci.* **2010**, *65*, 380–385, doi:10.1016/j.ces.2009.07.020.
7. Hessel, V.; Löb, P.; Holger, L. *Industrial and Real-Life Applications of Micro-Reactor Process Engineering for Fine and Functional Chemistry*; Elsevier: Amsterdam, The Netherlands, 2006; Volume 159, pp. 35–46.
8. Ouyang, X.; Besser, R.S. Development of a microreactor-based parallel catalyst analysis system for synthesis gas conversion. *Catal. Today* **2003**, *84*, 33–41, doi:10.1016/S0920-5861(03)00298-0.
9. Gavriilidis, A.; Angeli, P.; Cao, E.; Yeong, K.K.; Wan, Y.S.S. Technology and Applications of Microengineered Reactors. *Chem. Eng. Res. Design* **2002**, *80*, 3–30, doi:10.1205/026387602753393196.
10. Myrstad, R.; Eri, S.; Pfeifer, P.; Rytter, E.; Holmen, A. Fischer-Tropsch synthesis in a microstructured reactor. *Catal. Today* **2009**, *147*, S301–S304, doi:10.1016/j.cattod.2009.07.011.
11. LeViness, S.; Deshmukh, S.R.; Richard, L.A.; Robota, H.J. Velocys Fischer—Tropsch synthesis technology—New advances on state-of-the-art. *Top. Catal.* **2014**, *57*, 518–525.
12. Mazanec, T.; Perry, S.; Tonkovich, L.; Wang, Y. Microchannel gas-to-liquids conversion-thinking big by thinking small. In *Studies in Surface Science and Catalysis*; Elsevier: Amsterdam, The Netherlands, 2004; Volume 147, pp. 169–174.
13. Deshmukh, S.R.; Tonkovich, A.L.Y.; Jarosch, K.T.; Schrader, L.; Fitzgerald, S.P.; Kilanowski, D.R.; Lerou, J.J.; Mazanec, T.J. Scale-up of microchannel reactors for Fischer—Tropsch synthesis. *Ind. Eng. Chem. Res.* **2010**, *49*, 10883–10888.
14. Almeida, L.C.; Sanz, O.; D'olhaberriague, J.; Yunes, S.; Montes, M. Microchannel reactor for Fischer—Tropsch synthesis: Adaptation of a commercial unit for testing microchannel blocks. *Fuel* **2013**, *110*, 171–177.
15. Schulz, H. Short history and present trends of Fischer—Tropsch synthesis. *Appl. Catal. A Gen.* **1999**, *186*, 3–12, doi:10.1016/S0926-860X(99)00160-X.
16. Borg, Ø.; Eri, S.; Blekkan, E.A.; Storsæter, S.; Wigum, H.; Rytter, E.; Holmen, A. Fischer—Tropsch synthesis over γ-alumina-supported cobalt catalysts: Effect of support variables. *J. Catal.* **2007**, *248*, 89–100.
17. Chu, W.; Chernavskii, P.A.; Gengembre, L.; Pankina, G.A.; Fongarland, P.; Khodakov, A.Y. Cobalt species in promoted cobalt alumina-supported Fischer—Tropsch catalysts. *J. Catal.* **2007**, *252*, 215–230.
18. Hilmen, A.; Schanke, D.; Hanssen, K.; Holmen, A. Study of the effect of water on alumina supported cobalt Fischer—Tropsch catalysts. *Appl. Catal. A Gen.* **1999**, *186*, 169–188.
19. Storsæter, S.; Tøtdal, B.; Walmsley, J.C.; Tanem, B.S.; Holmen, A. Characterization of alumina-, silica-, and titania-supported cobalt Fischer—Tropsch catalysts. *J. Catal.* **2005**, *236*, 139–152.
20. Hilmen, A.; Schanke, D.; Holmen, A. TPR study of the mechanism of rhenium promotion of alumina-supported cobalt Fischer-Tropsch catalysts. *Catal. Lett.* **1996**, *38*, 143–147.
21. Morales, F.; De Groot, F.M.; Gijzeman, O.L.; Mens, A.; Stephan, O.; Weckhuysen, B.M. Mn promotion effects in Co/TiO_2 Fischer—Tropsch catalysts as investigated by XPS and STEM-EELS. *J. Catal.* **2005**, *230*, 301–308.
22. Iglesia, E.; Soled, S.L.; Fiato, R.A. Fischer-Tropsch synthesis on cobalt and ruthenium. Metal dispersion and support effects on reaction rate and selectivity. *J. Catal.* **1992**, *137*, 212–224.
23. Li, J.; Coville, N.J. The effect of boron on the catalyst reducibility and activity of Co/TiO_2 Fischer—Tropsch catalysts. *Appl. Catal. A Gen.* **1999**, *181*, 201–208.
24. Feltes, T.E.; Espinosa-Alonso, L.; De Smit, E.; D'Souza, L.; Meyer, R.J.; Weckhuysen, B.M.; Regalbuto, J.R. Selective adsorption of manganese onto cobalt for optimized $Mn/Co/TiO_2$ Fischer—Tropsch catalysts. *J. Catal.* **2010**, *270*, 95–102.
25. Li, J.; Jacobs, G.; Zhang, Y.; Das, T.; Davis, B.H. Fischer—Tropsch synthesis: Effect of small amounts of boron, ruthenium and rhenium on Co/TiO_2 catalysts. *Appl. Catal. A Gen.* **2002**, *223*, 195–203.
26. Arai, H.; Mitsuishi, K.; Seiyama, T. TiO_2-supported fe–co, co–ni, and ni–fe alloy catalysts for fischer-tropsch synthesis. *Chem. Lett.* **1984**, *13*, 1291–1294.
27. Duvenhage, D.; Coville, N. Fe: Co/TiO2 bimetallic catalysts for the Fischer—Tropsch reaction: Part 2. The effect of calcination and reduction temperature. *Appl. Catal. A Gen.* **2002**, *233*, 63–75.
28. Ying, X.; Zhang, L.; Xu, H.; Ren, Y.-L.; Luo, Q.; Zhu, H.-W.; Qu, H.; Xuan, J. Efficient Fischer—Tropsch microreactor with innovative aluminizing pretreatment on stainless steel substrate for Co/Al_2O_3 catalyst coating. *Fuel Process. Technol.* **2016**, *143*, 51–59, doi:10.1016/j.fuproc.2015.11.005.
29. Ernst, B.; Libs, S.; Chaumette, P.; Kiennemann, A. Preparation and characterization of Fischer—Tropsch active Co/SiO_2 catalysts. *Appl. Catal. A Gen.* **1999**, *186*, 145–168.

30. Li, J.; Jacobs, G.; Das, T.; Zhang, Y.; Davis, B. Fischer—Tropsch synthesis: Effect of water on the catalytic properties of a Co/SiO_2 catalyst. *Appl. Catal. A Gen.* **2002**, *236*, 67–76.
31. Barbier, A.; Tuel, A.; Arcon, I.; Kodre, A.; Martin, G.A. Characterization and catalytic behavior of Co/SiO_2 catalysts: Influence of dispersion in the Fischer—Tropsch reaction. *J. Catal.* **2001**, *200*, 106–116.
32. Yang, Y.; Xiang, H.-W.; Tian, L.; Wang, H.; Zhang, C.-H.; Tao, Z.-C.; Xu, Y.-Y.; Zhong, B.; Li, Y.-W. Structure and Fischer—Tropsch performance of iron—Manganese catalyst incorporated with SiO_2. *Appl. Catal. A Gen.* **2005**, *284*, 105–122.
33. Moradi, G.; Basir, M.; Taeb, A.; Kiennemann, A. Promotion of Co/SiO_2 Fischer—Tropsch catalysts with zirconium. *Catal. Commun.* **2003**, *4*, 27–32.
34. Chen, W.; Fan, Z.; Pan, X.; Bao, X. Effect of confinement in carbon nanotubes on the activity of Fischer—Tropsch iron catalyst. *J. Am. Chem. Soc.* **2008**, *130*, 9414–9419.
35. Bahome, M.C.; Jewell, L.L.; Hildebrandt, D.; Glasser, D.; Coville, N.J. Fischer—Tropsch synthesis over iron catalysts supported on carbon nanotubes. *Appl. Catal. A Gen.* **2005**, *287*, 60–67.
36. Abbaslou, R.M.M.; Tavassoli, A.; Soltan, J.; Dalai, A.K. Iron catalysts supported on carbon nanotubes for Fischer—Tropsch synthesis: Effect of catalytic site position. *Appl. Catal. A Gen.* **2009**, *367*, 47–52.
37. Nagineni, V.S.; Zhao, S.; Potluri, A.; Liang, Y.; Siriwardane, U.; Seetala, N.V.; Fang, J.; Palmer, J.; Kuila, D. Microreactors for Syngas Conversion to Higher Alkanes: Characterization of Sol−Gel-Encapsulated Nanoscale Fe−Co Catalysts in the Microchannels. *Ind. Eng. Chem. Res.* **2005**, *44*, 5602–5607, doi:10.1021/ie0487484.
38. Mehta, S.; Deshmane, V.; Zhao, S.; Kuila, D. Comparative Studies of Silica-Encapsulated Iron, Cobalt, and Ruthenium Nanocatalysts for Fischer—Tropsch Synthesis in Silicon-Microchannel Microreactors. *Ind. Eng. Chem. Res.* **2014**, *53*, 16245–16253, doi:10.1021/ie502193e.
39. Zhao, S.; Nagineni, V.S.; Seetala, N.V.; Kuila, D. Microreactors for Syngas Conversion to Higher Alkanes: Effect of Ruthenium on Silica-Supported Iron−Cobalt Nanocatalysts. *Ind. Eng. Chem. Res.* **2008**, *47*, 1684–1688, doi:10.1021/ie070967c.
40. Abrokwah, R.Y.; Rahman, M.M.; Deshmane, V.G.; Kuila, D. Effect of titania support on Fischer-Tropsch synthesis using cobalt, iron, and ruthenium catalysts in silicon-microchannel microreactor. *Mol. Catal.* **2019**, *478*, 110566, doi:10.1016/j.mcat.2019.110566.
41. Gutmann, B.; Koeckinger, M.; Glotz, G.; Ciaglia, T.; Slama, E.; Zadravec, M.; Pfanner, S.; Gruber-Woelfler, H.; Maier, M.; Kappe, C.O. Design and 3D Printing of a Stainless Steel Reactor for Continuous Difluoromethylations Using Fluoroform. *React. Chem. Eng.* **2017**, *2*, doi:10.1039/C7RE00176B.
42. Monaghan, T.; Harding, M.J.; Harris, R.A.; Friel, R.J.; Christie, S.D. Customisable 3D printed microfluidics for integrated analysis and optimisation. *Lab Chip* **2016**, *16*, 3362–3373.
43. Scotti, G.; Matilainen, V.; Kanninen, P.; Piili, H.; Salminen, A.; Kallio, T.; Franssila, S. Laser additive manufacturing of stainless steel micro fuel cells. *J. Power Sources* **2014**, *272*, 356–361.
44. Scotti, G.; Kanninen, P.; Matilainen, V.-P.; Salminen, A.; Kallio, T. Stainless steel micro fuel cells with enclosed channels by laser additive manufacturing. *Energy* **2016**, *106*, 475–481.
45. Capel, A.J.; Edmondson, S.; Christie, S.D.; Goodridge, R.D.; Bibb, R.J.; Thurstans, M. Design and additive manufacture for flow chemistry. *Lab Chip* **2013**, *13*, 4583–4590.
46. Amin, R.; Knowlton, S.; Hart, A.; Yenilmez, B.; Ghaderinezhad, F.; Katebifar, S.; Messina, M.; Khademhosseini, A.; Tasoglu, S. 3D-printed microfluidic devices. *Biofabrication* **2016**, *8*, 022001.
47. Reintjens, R.; Ager, D.J.; De Vries, A.H. Flow chemistry, how to bring it to industrial scale? *Chim. Oggi* **2015**, *33*, 21–24.
48. Abrokwah, R.Y.; Deshmane, V.G.; Kuila, D. Comparative performance of M-MCM-41 (M: Cu, Co, Ni, Pd, Zn and Sn) catalysts for steam reforming of methanol. *J. Mol. Catal. A Chem.* **2016**, *425*, 10–20, doi:10.1016/j.molcata.2016.09.019.
49. Deshmane, V.G.; Abrokwah, R.Y.; Kuila, D. Synthesis of stable Cu-MCM-41 nanocatalysts for H_2 production with high selectivity via steam reforming of methanol. *Int. J. Hydrogen Energy* **2015**, *40*, 10439–10452, doi:10.1016/j.ijhydene.2015.06.084.
50. Abrokwah, R.Y.; Deshmane, V.G.; Owen, S.L.; Kuila, D. Cu-Ni Nanocatalysts in Mesoporous MCM-41 and TiO_2 to Produce Hydrogen for Fuel Cells via Steam Reforming Reactions. *Adv. Mater. Res.* **2015**, *1096*, 161–168, doi:10.4028/www.scientific.net/AMR.1096.161.
51. Tatineni, B.; Basova, Y.; Rahman, A.; Islam, S.; Rahman, M.; Islam, A.; Perkins, J.; King, J.; Taylor, J.; Kumar, D.; et al. Development of Mesoporous Silica Encapsulated Pd-Ni Nanocatalyst for Hydrogen Production.

In *Production and Purification of Ultraclean Transportation Fuels*; American Chemical Society: Washington DC, 2011; Volume 1088, pp. 177–190.

52. Taghizadeh, M.; Akhoundzadeh, H.; Rezayan, A.; Sadeghian, M. Excellent catalytic performance of 3D-mesoporous KIT-6 supported Cu and Ce nanoparticles in methanol steam reforming. *Int. J. Hydrogen Energy* **2018**, *43*, 10926–10937.
53. Lanzafame, P.; Perathoner, S.; Centi, G.; Frusteri, F. Synthesis and characterization of Co-containing SBA-15 catalysts. *J. Porous Mater.* **2007**, *14*, 305–313, doi:10.1007/s10934-006-9068-0.
54. Sing, K.S. Reporting physisorption data for gas/solid systems with special reference to the determination of surface area and porosity (Recommendations 1984). *Pure Appl. Chem.* **1985**, *57*, 603–619.
55. Biz, S.; Occelli, M.L. Synthesis and characterization of mesostructured materials. *Catal. Rev.* **1998**, *40*, 329–407.
56. Zhao, D.; Feng, J.; Huo, Q.; Melosh, N.; Fredrickson, G.H.; Chmelka, B.F.; Stucky, G.D. Triblock copolymer syntheses of mesoporous silica with periodic 50 to 300 angstrom pores. *Science* **1998**, *279*, 548–552.
57. Karthikeyan, G.; Pandurangan, A. Post synthesis alumination of KIT-6 materials with Ia3d symmetry and their catalytic efficiency towards multicomponent synthesis of 1H-pyrazolo[1,2-]phthalazine-5,10-dione carbonitriles and carboxylates. *J. Mol. Catal. A Chem.* **2012**, *361*, 58–67, doi:10.1016/j.molcata.2012.05.003.
58. Schwertmann, U.; Cambier, P.; Murad, E. Properties of Goethites of Varying Crystallinity. *Clays Clay Miner.* **1985**, *33*, 369–378, doi:10.1346/CCMN.1985.0330501.
59. Li, G.; Zhang, C.; Wang, Z.; Huang, H.; Peng, H.; Li, X. Fabrication of mesoporous Co_3O_4 oxides by acid treatment and their catalytic performances for toluene oxidation. *Appl. Catal. A Gen.* **2018**, *550*, 67–76, doi:10.1016/j.apcata.2017.11.003.
60. Liu, X.; He, J.; Yang, L.; Wang, Y.; Zhang, S.; Wang, W.; Wang, J. Liquid-phase oxidation of cyclohexane to cyclohexanone over cobalt-doped SBA-3. *Catal. Commun.* **2010**, *11*, 710–714, doi:10.1016/j.catcom.2010.01.026.
61. Li, Z.; Miao, Z.; Wang, X.; Zhao, J.; Zhou, J.; Si, W.; Zhuo, S. One-pot synthesis of ZrMo-KIT-6 solid acid catalyst for solvent-free conversion of glycerol to solketal. *Fuel* **2018**, *233*, 377–387.
62. Hess, C.; Tzolova-Müller, G.; Herbert, R. The Influence of Water on the Dispersion of Vanadia Supported on Silica SBA-15: A Combined XPS and Raman Study. *J. Phys. Chem. C* **2007**, *111*, 9471–9479, doi:10.1021/jp0713920.
63. Bhoware, S.S.; Singh, A.P. Characterization and catalytic activity of cobalt containing MCM-41 prepared by direct hydrothermal, grafting and immobilization methods. *J. Mol. Catal. A Chem.* **2007**, *266*, 118–130, doi:10.1016/j.molcata.2006.09.031.
64. Yao, Q.; Lu, Z.-H.; Yang, K.; Chen, X.; Zhu, M. Ruthenium nanoparticles confined in SBA-15 as highly efficient catalyst for hydrolytic dehydrogenation of ammonia borane and hydrazine borane. *Sci. Rep.* **2015**, *5*, 15186–15186, doi:10.1038/srep15186.
65. Panpranot, J.; Goodwin, J.G., Jr.; Sayari, A. Synthesis and characteristics of MCM-41 supported CoRu catalysts. *Catal. Today* **2002**, *77*, 269–284, doi:10.1016/S0920-5861(02)00252-3.
66. Martínez, A.; López, C.; Márquez, F.; Díaz, I. Fischer-Tropsch synthesis of hydrocarbons over mesoporous Co/SBA-15 catalysts: The influence of metal loading, cobalt precursor, and promoters. *J. Catal.* **2003**, *220*, 486–499, doi:10.1016/S0021-9517(03)00289-6.
67. Lim, S.; Ciuparu, D.; Yang, Y.; Du, G.; Pfefferle, L.D.; Haller, G.L. Improved synthesis of highly ordered Co-MCM-41. *Microporous Mesoporous Mater.* **2007**, *101*, 200–206, doi:10.1016/j.micromeso.2006.11.002.
68. Jiang, T.; Shen, W.; Zhao, Q.; Li, M.; Chu, J.; Yin, H. Characterization of CoMCM-41 mesoporous molecular sieves obtained by the microwave irradiation method. *J. Solid State Chem.* **2008**, *181*, 2298–2305, doi:10.1016/j.jssc.2008.05.010.
69. Haddad, G.J.; Goodwin, J.G., Jr. The impact of aqueous impregnation on the properties of prereduced vs. precalcined Co/SiO_2. *J. Catal.* **1995**, *157*, 25–34, doi:10.1006/jcat.1995.1264.
70. Cai, Q.; Li, J. Catalytic properties of the Ru promoted Co/SBA-15 catalysts for Fischer—Tropsch synthesis. *Catal. Commun.* **2008**, *9*, 2003–2006, doi:10.1016/j.catcom.2008.03.035.
71. Van Der Laan, G.P.; Beenackers, A. Kinetics and selectivity of the Fischer—Tropsch synthesis: A literature review. *Catal. Rev.* **1999**, *41*, 255–318.
72. Yates, I.C.; Satterfield, C.N. Intrinsic kinetics of the Fischer-Tropsch synthesis on a cobalt cvatalyst. *Energy Fuels* **1991**, *5*, 168–173.

73. Iglesia, E.; Reyes, S.C.; Soled, S.L. Reaction-transport selectivity models and the design of Fischer-Tropsch catalysts. *Chem. Ind.-N. Y.-Marcel Dekker-* **1993**, Volume 51, 199–257.
74. Zennaro, R.; Tagliabue, M.; Bartholomew, C.H. Kinetics of Fischer—Tropsch synthesis on titania-supported cobalt. *Catal. Today* **2000**, *58*, 309–319.
75. Das, T.K.; Conner, W.A.; Li, J.; Jacobs, G.; Dry, M.E.; Davis, B.H. Fischer–Tropsch synthesis: Kinetics and effect of water for a Co/SiO_2 catalyst. *Energy Fuels* **2005**, *19*, 1430–1439.
76. Almeida, L.; Sanz, O.; Merino, D.; Arzamendi, G.; Gandía, L.; Montes, M. Kinetic analysis and microstructured reactors modeling for the Fischer—Tropsch synthesis over a Co–Re/Al_2O_3 catalyst. *Catal. Today* **2013**, *215*, 103–111.
77. Yang, C.-H.; Massoth, F.; Oblad, A. Kinetics of CO+ H_2 reaction over Co–Cu–Al_2O_3 catalyst. Hydrocarbon synthesis from carbon monoxide and hydrogen. *J. Am. Chem. Soc.* **1979**, *178*, 35–46.
78. Pannell, R.B.; Kibby, C.L.; Kobylinski, T.P. A Steady-State Study of Fischer-Tropsch Product Distributions Over Cobalt, Iron and Ruthenium. In *Studies in Surface Science and Catalysis*; Seivama, T., Tanabe, K., Eds.; Elsevier: Amsterdam, The Netherlands, 1981; Volume 7, pp. 447–459.
79. Outi, A.; Rautavuoma, I.; Van der Baan, H.S. Kinetics and mechanism of the fischer tropsch hydrocarbon synthesis on a cobalt on alumina catalyst. *Appl. Catal.* **1981**, *1*, 247–272, doi:10.1016/0166-9834(81)80031-0.
80. Sun, Y.; Jia, Z.; Yang, G.; Zhang, L.; Sun, Z. Fischer-Tropsch synthesis using iron based catalyst in a microchannel reactor: Performance evaluation and kinetic modeling. *Int. J. Hydrogen Energy* **2017**, *42*, 29222–29235, doi:10.1016/j.ijhydene.2017.10.022.
81. Mirzaei, A.A.; Kiai, R.M.; Atashi, H.; Arsalanfar, M.; Shahriari, S. Kinetic study of CO hydrogenation over co-precipitated iron–nickel catalyst. *J. Ind. Eng. Chem.* **2012**, *18*, 1242–1251, doi:10.1016/j.jiec.2012.01.003.
82. Sarup, B.; Wojciechowski, B.W. Studies of the fischer-tropsch synthesis on a cobalt catalyst II. Kinetics of carbon monoxide conversion to methane and to higher hydrocarbons. *Can. J. Chem. Eng.* **1989**, *67*, 62–74, doi:10.1002/cjce.5450670110.
83. Bepari, S.; Pradhan, N.C.; Dalai, A.K. Selective production of hydrogen by steam reforming of glycerol over Ni/Fly ash catalyst. *Catal. Today* **2017**, *291*, 36–46, doi:10.1016/j.cattod.2017.01.015.
84. Fogler, H.S. *Elements of Chemical Reaction Engineering*, 3rd ed.; Prentice Hall PTR: Upper Saddle River, NJ, USA, 1999.
85. Van Santen, R.A.; Ciobîcâ, I.M.; Van Steen, E.; Ghouri, M.M. Mechanistic Issues in Fischer-Tropsch Catalysis. In *Advances in Catalysis*; Academic Press: Cambridge, MA, USA, 2011; Volume 54, pp. 127–187.
86. Van Santen, R.A.; Ghouri, M.M.; Shetty, S.; Hensen, E.M.H. Structure sensitivity of the Fischer-Tropsch reaction; Molecular kinetics simulations. *Catal. Sci. Technol.* **2011**, *1*, 891–911, doi:10.1039/c1cy00118c.
87. Markvoort, A.J.; Van Santen, R.A.; Hilbers, P.A.J.; Hensen, E.J.M. Kinetics of the Fischer-Tropsch reaction. *Angew. Chem.-Int. Ed.* **2012**, *51*, 9015–9019, doi:10.1002/anie.201203282.
88. Mansouri, M.; Atashi, H.; Mirzaei, A.A.; Jangi, R. Kinetics of the Fischer-Tropsch synthesis on silica-supported cobalt-cerium catalyst. *Int. J. Ind. Chem.* **2013**, *4*, 1, doi:10.1186/2228-5547-4-1.
89. Pant, K.K.; Upadhyayula, S. Detailed kinetics of Fischer Tropsch synthesis over Fe-Co bimetallic catalyst considering chain length dependent olefin desorption. *Fuel* **2019**, *236*, 1263–1272, doi:10.1016/j.fuel.2018.09.087.
90. Mosayebi, A.; Abedini, R. Detailed kinetic study of Fischer—Tropsch synthesis for gasoline production over CoNi/HZSM-5 nano-structure catalyst. *Int. J. Hydrogen Energy* **2017**, *42*, 27013–27023, doi:10.1016/j.ijhydene.2017.09.060.
91. Abbasi, M.; Mirzaei, A.A.; Atashi, H. The mechanism and kinetics study of Fischer–Tropsch reaction over iron-nickel-cerium nano-structure catalyst. *Int. J. Hydrogen Energy* **2019**, *44*, 24667–24679, doi:10.1016/j.ijhydene.2019.07.222.
92. Sun, Y.; Wei, J.; Zhang, J.P.; Yang, G. Optimization using response surface methodology and kinetic study of Fischer—Tropsch synthesis using SiO_2 supported bimetallic Co–Ni catalyst. *J. Nat. Gas Sci. Eng.* **2016**, *28*, 173–183.
93. Sun, Y.; Yang, G.; Zhang, L.; Sun, Z. Fischer-Tropsch synthesis in a microchannel reactor using mesoporous silica supported bimetallic Co-Ni catalyst: Process optimization and kinetic modeling. *Chem. Eng. Proc. Process Intensif.* **2017**, *119*, 44–61, doi:10.1016/j.cep.2017.05.017.
94. Moazami, N.; Wyszynski, M.L.; Rahbar, K.; Tsolakis, A.; Mahmoudi, H. A comprehensive study of kinetics mechanism of Fischer-Tropsch synthesis over cobalt-based catalyst. *Chem. Eng. Sci.* **2017**, *171*, 32–60.

95. Moazami, N.; Wyszynski, M.L.; Mahmoudi, H.; Tsolakis, A.; Zou, Z.; Panahifar, P.; Rahbar, K. Modelling of a fixed bed reactor for Fischer—Tropsch synthesis of simulated N_2-rich syngas over Co/SiO_2: Hydrocarbon production. *Fuel* **2015**, *154*, 140–151.
96. Marchese, M.; Heikkinen, N.; Giglio, E.; Lanzini, A.; Lehtonen, J.; Reinikainen, M. Kinetic Study Based on the Carbide Mechanism of a Co-Pt/γ-Al_2O_3 Fischer—Tropsch Catalyst Tested in a Laboratory-Scale Tubular Reactor. *Catalysts* **2019**, *9*, 717, doi:10.3390/catal9090717.
97. Bhatelia, T.; Li, C.e.; Sun, Y.; Hazewinkel, P.; Burke, N.; Sage, V. Chain length dependent olefin re-adsorption model for Fischer—Tropsch synthesis over Co-Al_2O_3 catalyst. *Fuel Process. Technol.* **2014**, *125*, 277–289, doi:10.1016/j.fuproc.2014.03.028.
98. Todic, B.; Bhatelia, T.; Froment, G.F.; Ma, W.; Jacobs, G.; Davis, B.H.; Bukur, D.B. Kinetic Model of Fischer—Tropsch Synthesis in a Slurry Reactor on Co–Re/Al_2O_3 Catalyst. *Ind. Eng. Chem. Res.* **2013**, *52*, 669–679, doi:10.1021/ie3028312.
99. Jahangiri, H.; Bennett, J.; Mahjoubi, P.; Wilson, K.; Gu, S. A review of advanced catalyst development for Fischer—Tropsch synthesis of hydrocarbons from biomass derived syn-gas. *Catal. Sci. Technol.* **2014**, *4*, 2210–2229, doi:10.1039/C4CY00327F.
100. Iglesia, E. Design, synthesis, and use of cobalt-based Fischer-Tropsch synthesis catalysts. *Appl. Catal. A Gen.* **1997**, *161*, 59–78, doi:10.1016/S0926-860X(97)00186-5.
101. Iglesia, E.; Soled, S.L.; Fiato, R.A.; Via, G.H. Bimetallic Synergy in Cobalt Ruthenium Fischer-Tropsch Synthesis Catalysts. *J. Catal.* **1993**, *143*, 345–368, doi:10.1006/jcat.1993.1281.
102. Kleitz, F.; Choi, S.H.; Ryoo, R. Cubic Ia 3 d large mesoporous silica: Synthesis and replication to platinum nanowires, carbon nanorods and carbon nanotubes. *Chem. Commun.* **2003**, *17*, 2136–2137.
103. Barrett, E.P.; Joyner, L.G.; Halenda, P.P. The Determination of Pore Volume and Area Distributions in Porous Substances. I. Computations from Nitrogen Isotherms. *J. Am. Chem. Soc.* **1951**, *73*, 373–380, doi:10.1021/ja01145a126.